

ADVERTIMENT. La consulta d'aquesta tesi queda condicionada a l'acceptació de les següents condicions d'ús: La difusió d'aquesta tesi per mitjà del servei TDX (www.tesisenxarxa.net) ha estat autoritzada pels titulars dels drets de propietat intel·lectual únicament per a usos privats emmarcats en activitats d'investigació i docència. No s'autoritza la seva reproducció amb finalitats de lucre ni la seva difusió i posada a disposició des d'un lloc aliè al servei TDX. No s'autoritza la presentació del seu contingut en una finestra o marc aliè a TDX (framing). Aquesta reserva de drets afecta tant al resum de presentació de la tesi com als seus continguts. En la utilització o cita de parts de la tesi és obligat indicar el nom de la persona autora.

ADVERTENCIA. La consulta de esta tesis queda condicionada a la aceptación de las siguientes condiciones de uso: La difusión de esta tesis por medio del servicio TDR (www.tesisenred.net) ha sido autorizada por los titulares de los derechos de propiedad intelectual únicamente para usos privados enmarcados en actividades de investigación y docencia. No se autoriza su reproducción con finalidades de lucro ni su difusión y puesta a disposición desde un sitio ajeno al servicio TDR. No se autoriza la presentación de su contenido en una ventana o marco ajeno a TDR (framing). Esta reserva de derechos afecta tanto al resumen de presentación de la tesis como a sus contenidos. En la utilización o cita de partes de la tesis es obligado indicar el nombre de la persona autora.

WARNING. On having consulted this thesis you're accepting the following use conditions: Spreading this thesis by the TDX (www.tesisenxarxa.net) service has been authorized by the titular of the intellectual property rights only for private uses placed in investigation and teaching activities. Reproduction with lucrative aims is not authorized neither its spreading and availability from a site foreign to the TDX service. Introducing its content in a window or frame foreign to the TDX service is not authorized (framing). This rights affect to the presentation summary of the thesis as well as to its contents. In the using or citation of parts of the thesis it's obliged to indicate the name of the author

Doctoral Thesis

NUMERICAL ANALYSIS
OF CONCRETE-FILLED TUBES WITH STIFFENING PLATES
UNDER LARGE DEFORMATION AXIAL LOADING

phD student
Albert Albareda Valls

Directed by
Dr. Jordi Maristany Carreras

June 2012

Chapter VI

PARAMETRIC ANALYSIS

This Chapter, together with Chapter VII, constitutes the main body of this investigation.

Main objective of this Chapter is to present the results obtained from the parametric analysis which have been carried out. A set of 30 different specimens have been analyzed under large deformation axial loading, separated by five different typologies depending on geometry and material strengths.

After defining the mechanical and geometrical features of specimens considered, a complete description of behavior of the two components [steel and concrete] and the contact in the interface is shown below.

The evolution of compressive damage in concrete core is also described and commented below. In addition, the damage dissipation energy is superimposed to the stress-strain diagrams in order to describe the process of energy absorption.

These results are presented separately depending on the geometry of each typology. Therefore, results coming from circular sections are presented in Section 6.2, and results coming from square sections are presented in Section 6.3.

Chapter VI

PARAMETRIC ANALYSIS

6.1 Analyzed designs.

6.1.1 Introduction to concrete-filled tubes stiffened with plates.

6.1.2 Analyzed typologies.

6.2 Large deformation axial loading behavior of circular reticulated CFT sections.

6.2.1 Geometrical features of the analysis.

6.2.2 General compressive response and ductility.

6.2.3 Tensional behavior of components.

6.2.4 Damage evolutionary analysis of concrete.

6.2.5 Analysis of contact pressure.

6.3 Large deformation axial loading behavior of square-shaped reticulated CFT sections.

6.3.1 Geometrical features of the analysis.

6.3.2 General compressive response and ductility.

6.3.3 Tensional behavior of components.

6.3.4 Damage evolutionary analysis of concrete.

6.3.5 Analysis of contact pressure.

6.1 Analyzed designs

6.1.1 Introduction to concrete-filled tubes stiffened with plates.

As it has been already exposed in previous Chapters, this investigation proposes the analysis of a specific typology of concrete-filled tubes, especially thought for tall buildings of seismic areas: "Concrete-filled tubes stiffened with plates" or "Reticulated concrete-filled tubes". This investigation is especially devoted to describe their behavior under large deformation axial loading.

Reticulated concrete-filled tubes make the most of its geometry, by "encapsulating" concrete filling in independent loading cells and contributing this way to the enhancement of confinement effect. Besides, their reticulated shape helps to absorb better the shear forces¹, thanks to the distribution of the steel plates in grid-shape in the cross-section. The fact of being formed by independent cells, similar to the natural shape of a swarm of bees, makes possible that each individual alveoli can work also separately, by confining the sandwiched concrete filling.

6.1.2 Analyzed typologies.

For comparison purpose, a parametric analysis of 30 different reticulated sections is proposed in this investigation, depending on geometry and materials. It pretends to provide a global description of their compressive behavior and to suggest some general design criteria, more than proposing universal application laws.

The most important criterion used to choose the typologies to analyze is based on the configuration of the plates: for circular sections, only two different typologies² have been proposed: C2 with two, and C4 with four different circular sectors. In order to cover some possible differences in the behavior by considering different wall-thicknesses, two different groups per each typology have been proposed in the analysis: specimens made of 10 mm tube wall-thickness, and specimens made of 5 mm tube wall-thickness. The stiffening plates embedded in the core have been always assumed 1.20 times thicker than the tube, basically for two different reasons:

- As it has been noted in Section 3.2.5, the thickness of stiffening plates has no influence on the deformability of circular tubes [obviously, in case of usual thicknesses]. Similar is its influence on square-shaped tubes, although in this case stiffening plates absorb part of the confining pressure [Fig. III.34]; in addition, the thickness of stiffening plates plays a significant role in determining the flexural rigidity of the plates: however, from values of thickness equivalent to the tube wall, this influence vanishes [see Fig. III.31]. This is the first reason why these plates have been considered 1.20 thicker than the tubes.
- The assumption of different thicknesses of stiffening plates, combined with the rest of variables would lead to a too vast parametric study, with few variations in results. Thus, as this investigation has been more focused on a descriptive analysis than on obtaining some specific universal laws, the thickness of these plates have been considered constant.

Besides, a set of four equivalent circular-shaped specimens have been also modeled; this way, the area of steel disposed in their homologous stiffened sections coincides exactly with that of these equivalent circular tubes, with a theoretical thickness of t_{eq} [see Tables VI.1 to VI.5].

The variations which generate final combinations not only come from the typology and geometry, but also from material strengths. Three different compressive strengths have been considered for

¹ a quality which is really important in basement columns of tall buildings

² for practical reasons

Chapter VI

Parametric analysis

concrete [30, 40 and 50 MPa], coinciding with low and mid strength concretes. Concrete of 50MPa is considered as mid-strength since columns of tall buildings may be designed with really higher strength concretes of 80 and 100MPa. However, these strengths show almost no residual stress after the peak of load [see figure IV.19], providing few ductility to the column. The study of reticulated sections, filled with high-strength concrete, has been proposed as a further investigation in Chapter VIII. Contrarily, a unique value of strength of steel has been assumed for the analysis [355 MPa]. Few differences are observed by using other structural steels.

Mechanical properties of stiffened circular sections [C2, C4 and their equivalents] are summarized in Tables VI.1 and VI.2, taking the following form:

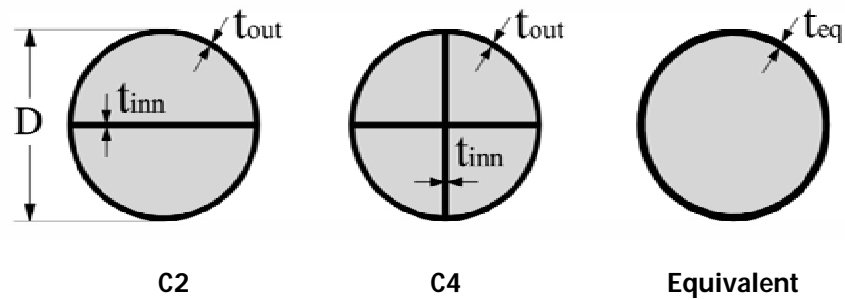


Fig. VI.1 Proposed reticulated circular typologies.

Nomenclature refers to the number of circular loading sectors, two and four.

Table VI.1 General features of specimens C2.

Model	D* [mm]	t _{out} * [mm]	t _{inn} * [mm]	t _{eq} * [mm]	f _c ** [MPa]	f _y ** [MPa]	D/t
C2a	400	10	12	14	30	355	40
C2b	400	10	12	14	40	355	40
C2c	400	10	12	14	50	355	40
C2d	400	5	6	7	30	355	80
C2e	400	5	6	7	40	355	80
C2f	400	5	6	7	50	355	80

Values expressed in mm* and MPa**.

Table VI.2 General features of specimens C4.

Model	D* [mm]	t _{out} * [mm]	t _{inn} * [mm]	t _{eq} * [mm]	f _c ** [MPa]	f _y ** [MPa]	D/t
C4a	400	10	12	14.4	30	355	40
C4b	400	10	12	14.4	40	355	40
C4c	400	10	12	14.4	50	355	40
C4d	400	5	6	7.2	30	355	80
C4e	400	5	6	7.2	40	355	80
C4f	400	5	6	7.2	50	355	80

Values are expressed in mm* and MPa*.

The proposed parametric analysis also involves the study of square-shaped tubes. In this case, the study of sections formed by two, four and nine different alveoli has been proposed, assuming that the denser is the grid, more similar is the behavior of the cells between them. Thus, the proposed and analyzed square-shaped typologies are the following:

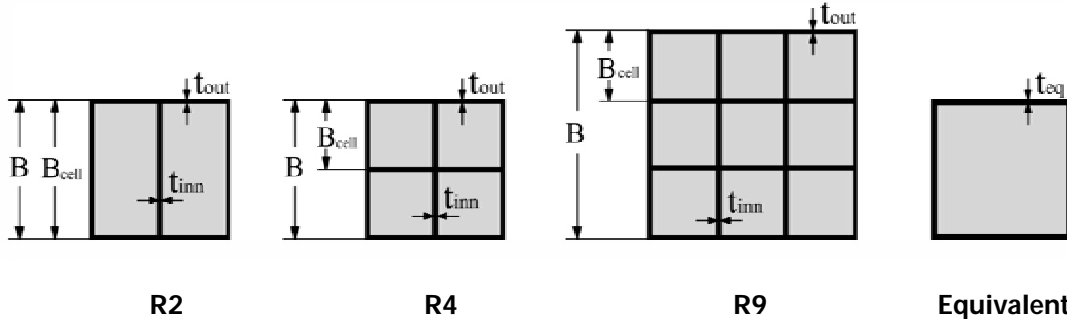


Fig. VI.2. Proposed stiffened square-shaped typologies.

Nomenclature refers to the number of loading cells, from two to nine.

The models proposed in the analysis have been thought for heavily loaded columns of tall buildings, with practical dimensions of 400 and 600 mm width; although parametric analysis is limited for evident reasons, the results can be easily extrapolated to other configurations with stronger requirements. Then, by assuming these outer dimensions, these independent loading cells have been considered of 200 mm width, a sufficient reduced size in order to guarantee the increment of confinement on the core in square-shaped sections. As a consequence, the B_{cell}/t ratios for sections R4 and R9 are 20 in sections 10mm thick, and 40 in sections 5mm thick, while these values grow up to 40 and 80 in case of section R2.

Table VI.3 General features of specimens R2.

Model	B^* [mm]	t_{out}^* [mm]	t_{int}^* [mm]	t_{eq}^* [mm]	f_c^{**} [MPa]	f_y^{**} [MPa]	B_{cell}/t
R2a	400	10	12	10/16	30	355	40
R2b	400	10	12	10/16	40	355	40
R2c	400	10	12	10/16	50	355	40
R2d	400	5	6	5/8	30	355	80
R2e	400	5	6	5/8	40	355	80
R2f	400	5	6	5/8	50	355	80

Values are expressed in mm* and MPa*.

Table VI.4 General features of specimens R4.

Model	B^* [mm]	t_{out}^* [mm]	t_{int}^* [mm]	t_{eq}^* [mm]	f_c^{**} [MPa]	f_y^{**} [MPa]	B_{cell}/t
R4a	400	10	12	16	30	355	20
R4b	400	10	12	16	40	355	20
R4c	400	10	12	16	50	355	20
R4d	400	5	6	8	30	355	40
R4e	400	5	6	8	40	355	40
R4f	400	5	6	8	50	355	40

Values are expressed in mm* and MPa*.

Table VI.5 General features of specimens R9.

Model	B*	t _{out} *	t _{int} *	t _{eq} *	f _c **	f _y **	B _{cell} /t
	[mm]	[mm]	[mm]	[mm]	[MPa]	[MPa]	
R9a	600	10	12	22	30	355	20
R9b	600	10	12	22	40	355	20
R9c	600	10	12	22	50	355	20
R9d	600	5	6	11	30	355	40
R9e	600	5	6	11	40	355	40
R9f	600	5	6	11	50	355	40

Values are expressed in mm* and MPa*.

Note that specimens of the first group [of 10mm wall-thickness] are clearly thick-walled, while those specimens of the second group [of 5mm wall-thickness] would be thin-walled, if stiffening plates would have not been introduced. The aim is to analyze sections with different B/t ratios, knowing that B is the width of the cell, named as B_{cell} , in order to check how stiffening plates affect the rigidity of these sections. Remember that thick-walled sections avoid local buckling effects in the elastic range, with B/t and D/t ratios well above the maximum limits established by (ENV1990-1-1, 1990), (Rondal, et al., 1996). These limit values correspond to:

$$\frac{B}{t} \leq 52 \cdot \varepsilon = 42.30 \quad (3.46)$$

for square or rectangular-shaped sections, and:

$$\frac{D}{t} \leq 90 \cdot \varepsilon^2 = 59.57 \quad (3.120)$$

for circular sections.

The European code does not specify any difference for these limits between hollow tubes and CFT sections, although it is evident that concrete filling plays a significant role in determining the slenderness of these tubes.

Once CFT sections have been stiffened, the unique section which clearly continues being over this limit is R2, with only one of the two sides, stiffened with a plate; also Section C2 would be excessively thin, in case of not considering the embedded stiffening plates. Theoretically, and according to (ENV1994-1-1, 1990), section C2 [d, e and f] is well above the limit value of 59.57, established by expression (3.120). However, this limit is oriented to circular hollow unstiffened tubes. In the FE results, local buckling before the yield limit stress of steel has been detected only in sections R2d, R2e and R2f [see further Sections].

It is obvious that a study of only six different specimens per typology is not really enough to cover a full parametric analysis to establish some universal laws for design practice. However, the final objective of this investigation is more oriented to describe the response of reticulated typologies under large deformation axial loading than to obtain universal application laws. Therefore, the

interest has been more focused on covering different typologies derived from the number and disposition of these plates, than on determining universal application formulas.

6.2 Large deformation axial loading behavior of circular reticulated CFT sections.

To carry out the proposed descriptive analysis of circular sections, twelve different specimens have been modeled depending on geometry and material strengths, according to the tables shown in Section 6.1. Besides, general modeling criteria defined in Chapter IV have been used to reproduce their behavior, especially knowing that experimental tests have not been carried out, strictly for practical reasons.

6.2.1 Geometrical features of the analysis.

According to Section 4.5.2.2, to analyze symmetrical sections until the collapse it is convenient to consider a generous size of the models, with a height of specimens approximately two times the width. Referring to boundary conditions, both loading faces have been considered restricted against rotation and lateral displacements in order to simplify the process and in order to obtain the closest similitude to experimental tests. Also the mesh size corresponds to those criteria which have been defined in Section 4.5.1, with a minimum of three different elements across the wall-thickness in order to be capable of reproducing local plastic buckling effects.

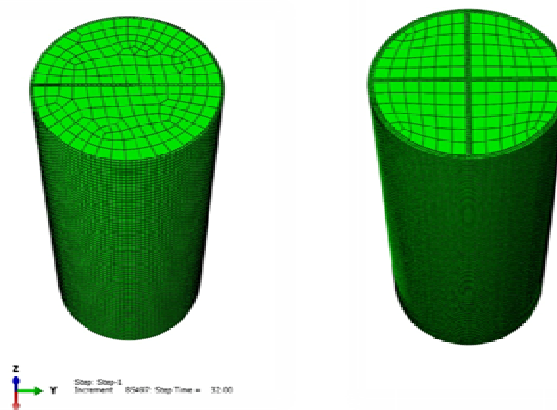


Fig. VI.3 Finite Element Mesh used for circular specimens.
Mesh size coincides with the criteria established in Chapter IV.

6.2.2 General compressive response and ductility.

Axial load diagrams depending on vertical strain are capable of describing the compressive behavior of a composite section in general terms, as well as the influence of material strengths and geometry. Although it will be necessary to carry out more detailed analyses of the behavior of components, it is evident that all circular CFT specimens show generous rates of ductility –stiffened or unstiffened, as it is derived from analysis presented in Chapter V.

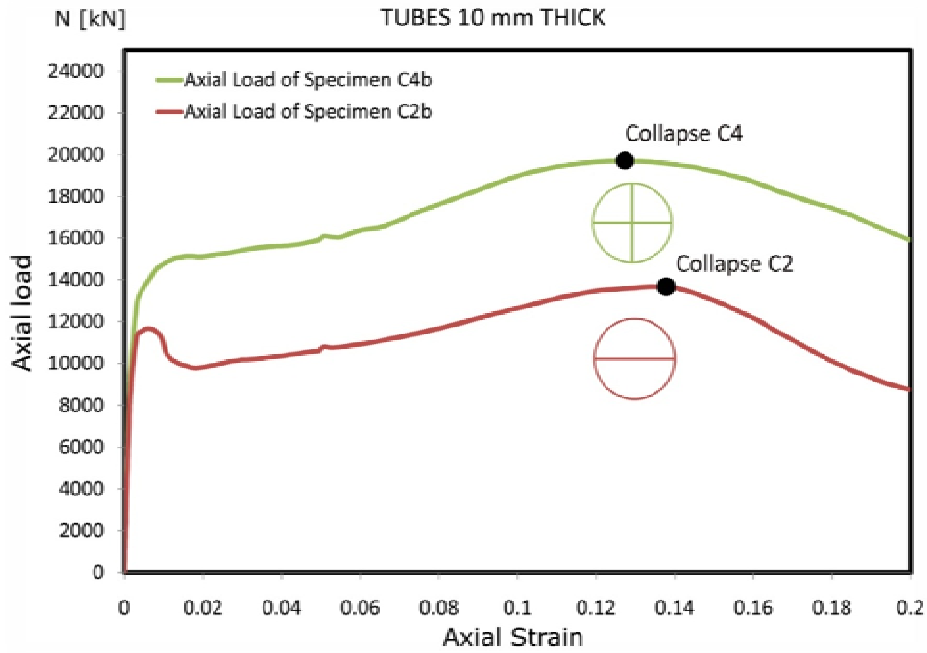


Fig. VI.4 General axial load-strain curves obtained from the FE analysis. Sections C2 and C4, of 10 mm wall-thickness [$D/t=40$].

Note from figure VI.4 that there is no enhancement of ductility between sections C2 and C4, even a slight decrement instead. This means that the fact of introducing stiffening plates in the core of circular CFT sections does not elongate the ultimate strain of these sections. The collapse of section C4 [with two stiffening plates] takes place at similar strain values as in section C2 or section CF4-CC40³, in which the failure occurs even earlier. However, the post-collapse descending branch is clearly softer in reticulated sections than in unstiffened tubes.

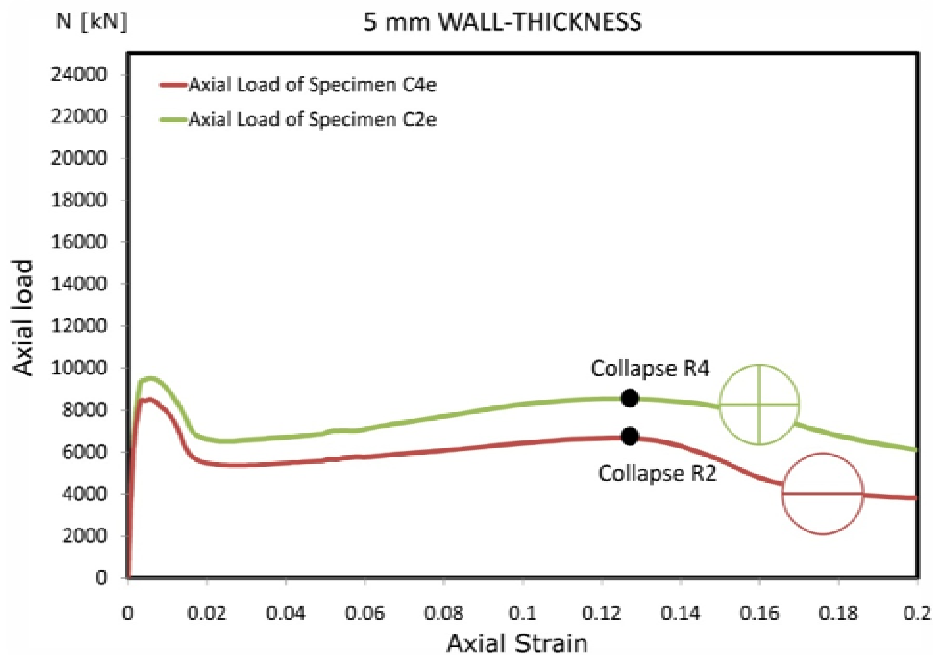


Fig. VI.5 General axial load-strain curves obtained from the FE analysis.

³ See figure V.13. Specimen CF4-CC40 comes from the investigation carried out by Susantha.

Sections C2 and C4, with 5 mm wall-thickness [D/t=80].

While in sections with low D/t ratios, the introduction of a second embedded plate⁴ contributes to eradicate part of the stiffness degradation of the core during the softening period, in sections with high D/t ratios, few differences between typologies C2 and C4 can be observed. May be the most significant divergence in the behavior is detected in the post-failure period: thin-walled sections with two stiffening plates [C4e] degrade really more softly than those with only one stiffening plate [C2e]. However, the ultimate load takes place at similar values of deformation.

Axial load-strain diagrams of sections C2e and C4e follow a surprisingly coincident path; variation between them comes only from the difference of the magnitude of absolute strength, due to the increment of confinement effect and area of steel. For analysis purpose, a set of "equivalent" proportional modules of the composite section have been calculated, according to each different period of the load-strain curve. These different periods correspond to E [elastic period], E_s [softening period], E_p [Plastic Hardening period], E_c [Collapse period] and E_r [Residual Stress]. These values have been obtained by dividing each load increment by the whole composite area, together with the corresponding growth of strain, according to expression 6.1 for any interval of the curve, i .

$$E_i = \frac{\Delta F_i}{A_{ac} \cdot \Delta \varepsilon_i} \quad (6.1)$$

These modules become valuable to do a quantitative description of the load-strain curve, as they express numerically the growing or the descendent tendency of the diagram.

The idealized diagram corresponding to these values is showed in figure VI.6. The first period is the elastic-plastic phase, being $[E]$ the secant modulus of the composite section. The second period belongs to the softening of concrete after the peak of load, being normally negative since the load usually tends to decrease during this phase $[E_s]$. The third period coincides with the plastic hardening of steel, where this component increases its strength until the failure and concrete becomes severely confined again $[E_p]$. The fourth period corresponds to the collapse of steel after plastic hardening period, during which the transference of stresses from the tube to the core takes place; normally, the failure of steel in circular concrete-filled tubes comes from the appearance of plastic local buckling in the tube $[E_c]$. Finally, the last period defined by E_r , describes the residual stress after the failure.

⁴ This is the case of section C4.

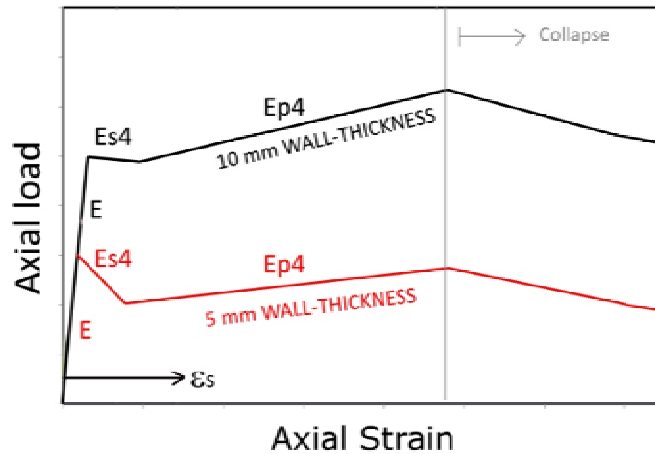


Fig. VI.6 Idealization of load-strain curves for circular sections.
Idealized proportional modules for 10mm thick-walled circular tubes [in black]
and 5mm thick-walled circular tubes [in red].

Table VI.6 Proportional modules of section C2.

Section C2	E2*	Es2*	Ep2*
C2b, $t_{out}=10\text{mm}$	15500	1135	245
C2e, $t_{out}=5\text{mm}$	15440	-1715	75

* All values expressed in N/mm².

Table VI.7 Proportional modules of section C4.

Section C4	E4*	Es4*	Ep4*
C4b, $t_{out}=10\text{mm}$	10100	0	380
C4e, $t_{out}=5\text{mm}$	15000	-1590	190

* All values expressed in N/mm².

Note how small the difference is between the descending branches of sections C2b and C2e in the softening period, while how significant it is between sections C4b and C4e. Also the hardening period is different for each typology: section C4 shows an important enhancement of strength, while this increment in section C2 is much more subtle. Note that the slope of residual stress of section C2 is zero [case C2e], or almost zero [case C2b], owing to the lack of rigidity of the tube.

6.2.3 Tensional behavior of components.

As in case of unstiffened circular CFT sections, the interaction between both components plays a decisive role in the compressive response. The performance of steel cannot be analyzed separately of the response of concrete, as the first is directly conditioned by the latter, and in reverse.

The steel tube in reticulated circular CFT sections behaves really similar as in unstiffened sections. The same load transferences between components described in Chapter V can be detected here, assuming that embedded stiffening plates provide a slight increment of confinement to the concrete

core. In the two following sequences, it is shown the evolution of combined von Mises stresses of the tube in section C2 from two different points of view.

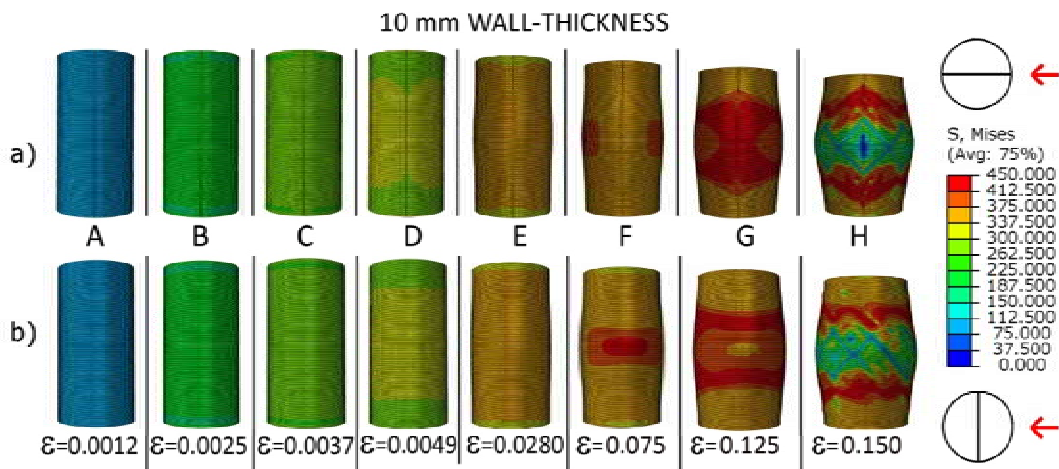


Fig. VI.7 Evolutionary sequence of von Mises stresses in C2b [10mm thick-walled].
Case a) refers to the view parallel to the inner plate and case b) refers to that perpendicular.

While in sections with low D/t ratios, the introduction of an extra stiffening plate does not have an explicit influence on the evolution of combined stresses and on the deformed shape, in sections with high D/t ratios, this extra plate becomes crucial. In these cases, it provides rigidity to the side corresponding to view a) in figure VI.8, and it avoids the appearance of local buckling in the nearby of the loading faces [see the last frame of sequence b)]. Note that although the D/t ratio in section C2e [80] is well above the maximum slenderness limit established by (ENV1990-1-1, 1990)⁵, the presence of this stiffening plate prevents from the appearance of buckling effects in the early stages of loading.

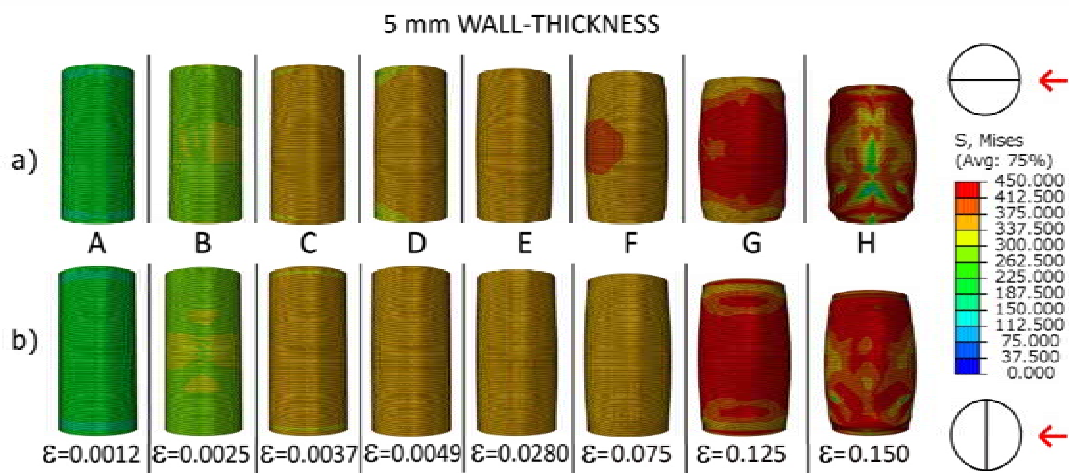


Fig. VI.8 Evolutionary sequence of von Mises stresses in C2e [5 mm thick-walled].
Case a) refers to the view parallel to the inner plate and case b) refers to the perpendicular.

Needless to say that the absorption of load in steel takes place really fast in the first stage of loading, while the evolution of vertical stress in concrete occurs with a certain delay respect to the first, due to the difference in their proportional modules. The stiffening effect provided by these

⁵ See expression (6.2)

plates becomes more explicit in section C4. The evolution of von Mises stress in steel in this case is represented in the sequence shown below [figure VI.9].

The fact of disposing two stiffening plates instead of only one tends to stiffen the shell homogenously, reducing this way the appearance of plastic buckling notably, by enhancing at the same time the compressive performance of the tube. Thus, both analyses corresponding to sections C4, with D/t ratios of 40 [C4b] and 80 [C4e], show quite similar deformed shapes:

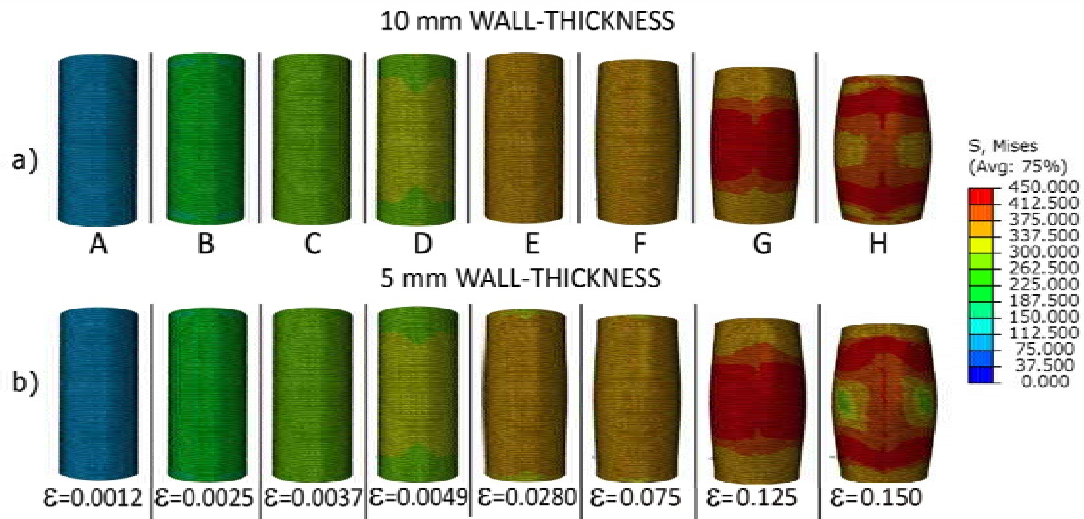


Fig. VI.9. Evolutionary sequence of von Mises stresses in section C4.
 Case a) refers to section C4b [10mm wall-thickness] and case b) refers to section C4e [5 mm wall-thickness].

Although the outer tube of section C2 is subjected to buckling effects in the plastic range, it can be clearly seen how one single stiffening plate reduces the wavelength of the deformed shape and, in some points, even can avoid the second-order effects [see those points of the tube close to the intersection with the embedded plate in figure VI.8]. On the contrary, in case of section C4, the deformed shape in *elephant foot* almost vanishes in all cases. Note how the plates embedded in concrete filling are fully restricted to buckling, and how they remain completely rigid until collapse. This phenomenon will be also detected, with some light differences, in the analyses corresponding to reticulated square-shaped sections, [see further Sections]. The truth is that, being not subjected to second-order effects, these embedded plates can absorb more percentage of load, resisting until the collapse. This phenomenon is observed in figure VI.10, where while the whole tube is subjected to an averaged vertical stress of approximately 200MPa, the stiffening plate has a tensional state well above this value [of 300 and 450 MPa].

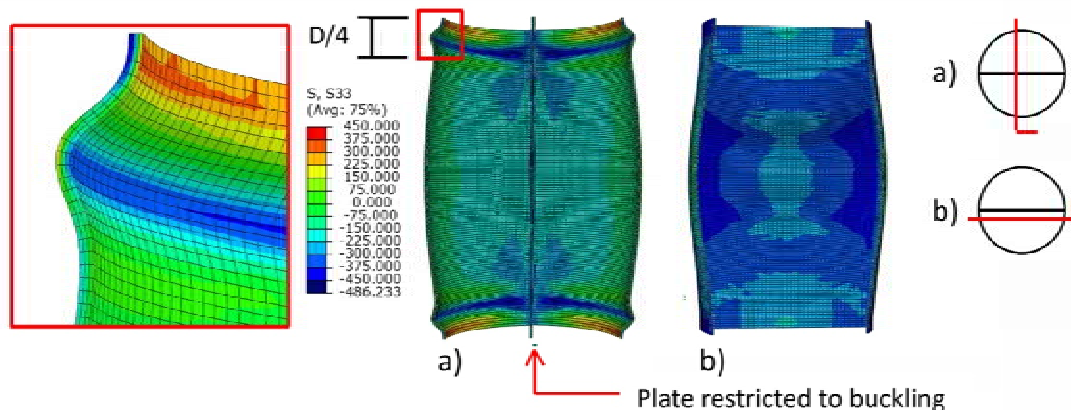


Fig. VI.10 Vertical stress of steel before the collapse, section C2e [5 mm wall-thickness]

Note that the restriction to buckling of the embedded plate allows reaching higher stresses.

In reticulated circular CFT sections, vertical stress of steel after yielding remains almost constant until the hardening period, by forming a wide horizontal plateau. The character of this yield plateau in thick-walled tubes depends basically on local buckling in the plastic range. Note that section C4 shows an important hardening period, while the existence of this period in section C2 depends basically on the D/t ratio.

Correspondence between vertical stress of steel and vertical stress of concrete becomes evident in curves of figures VI.11 and VI.12. The unique circular specimen that does not show a softening period after the peak of load is C4b, due to the important stiffness provided by the plates. Rigidity of the outer tube not only determines the stress of steel, but also it has a clear influence on the stress state of the core. It has been explained before that concrete subjected to high hydrostatic pressures softens more softly, even remaining constant in some cases.

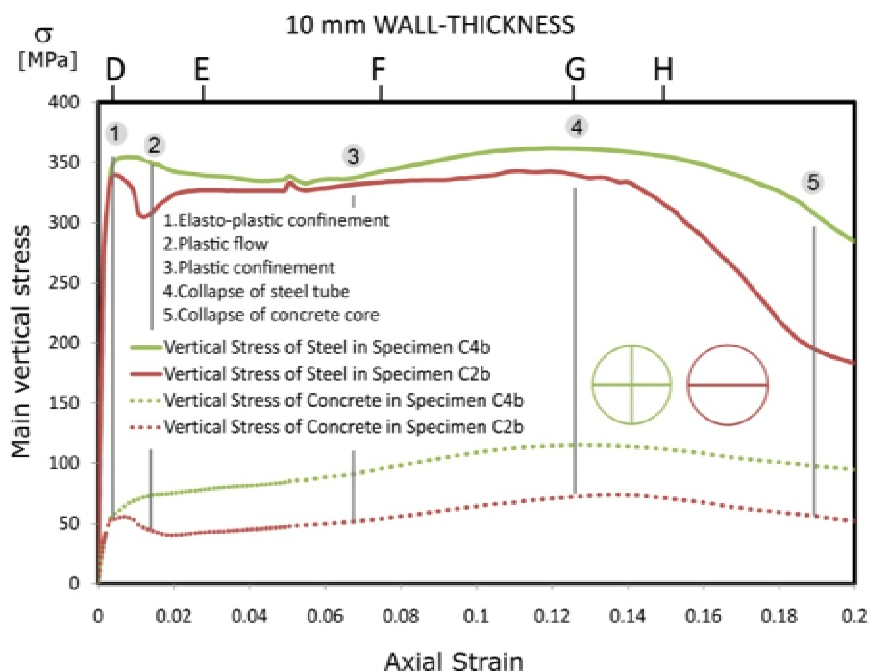


Fig. VI.11 Comparison between averaged vertical stress of steel and concrete in sections C2 and C4.

These curves correspond to sections with 10 mm wall-thickness.

The maximum values of vertical stress obtained for steel and concrete are summarized in the following two tables, VI.8 and VI.9. The nomenclature used for sections in these tables comes from Section 6.1.2 of this Chapter, where letters **a** and **d** correspond to a concrete filling of 30 MPa, **b** and **e** correspond to concrete of 40 MPa and letters **c** and **f** correspond to concrete of 50 MPa.

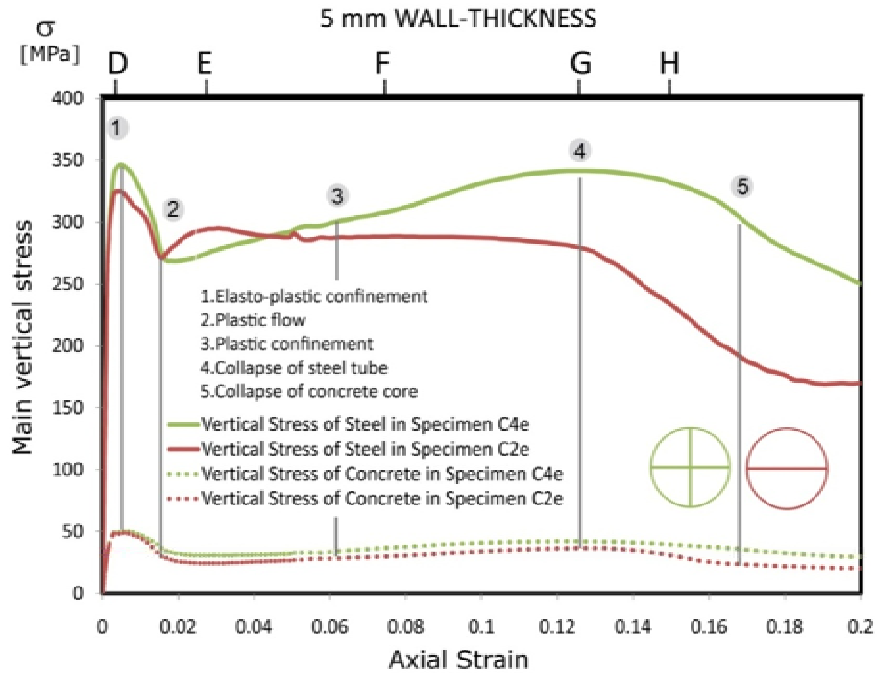


Fig. VI.12 Comparison between averaged vertical stress of steel and concrete in sections C2 and C4

These curves correspond to sections with 5 mm wall-thickness.

Table VI.8 Maximum vertical stress reached by steel*.

Section	a	b	c	d	e	f
f_{ck}	30	40	50	30	40	50
C2	337.93	339.33	342.62	322.98	325.09	327.47
C4	353.02	354.32	354.23	341.92	345.66	346.64

* All values expressed in N/mm².

Table VI.9 Maximum vertical stresses reached by concrete*.

Section	a	b	c	d	e	f
f_{ck}	30	40	50	30	40	50
C2	39.23	55.27	57.50	37.94	48.80	54.50
C4	57.27	74.47	77.30	41.35	51.90	58.21

* All values expressed in N/mm².

Contrarily to vertical stress, hoop stress in stiffened circular CFT sections behaves slightly different than in their homologous unstiffened sections. While in unstiffened circular sections the hoop stress is uniform and positive [tensile stress], in reticulated CFT sections this stress is not uniform across the wall-thickness owing to the cruciform geometry. When concrete expands laterally, the tube is clearly deformed outwards, only restricted by the stiffening plates of the core. This restriction implies the appearance of slight flexural stresses which leads to a reduction of ductility respect to the unstiffened CFT sections [see figure VI.14].

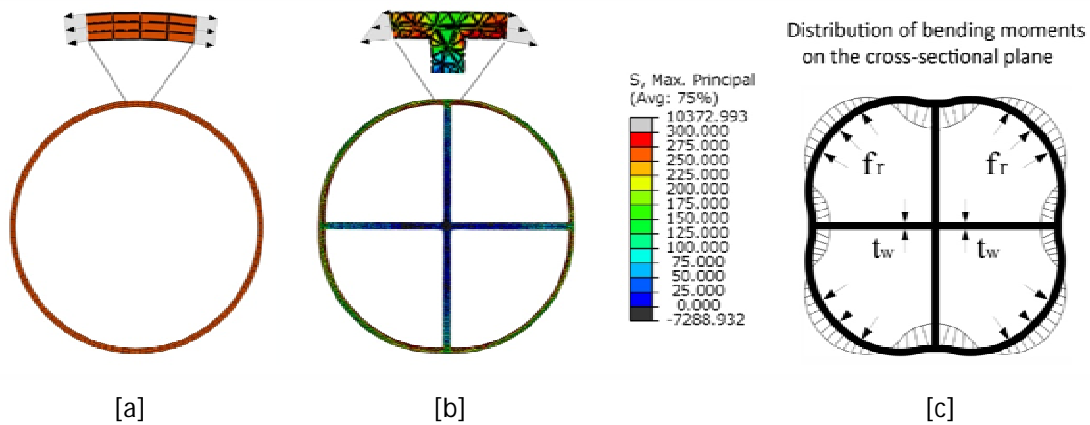


Fig. VI.14 Transversal stresses, σ_2 , in stiffened and unstiffened circular CFT sections.

[a] Unstiffened section CF4-CC40 [b] Stiffened section [C4b]

[c] Idealized distribution of bending moments in the cross-section.

The change from a circular geometry to a cruciform shape implies the appearance of slight flexural stresses in the cross-sectional plane.

This fact has been already predicted through the results from the preliminary 2-D elastic analysis in Chapter III. Note that the embedded plates are loaded vertically, but almost not loaded in the two axes of the cross-sectional plane. This is due basically to the effect of a circular geometry, which tends to absorb most part of the stress circumferentially. This way, stiffening plates play a secondary role in confining the concrete of the core, as they are not almost stressed in the [y] and [z] axes; this is the reason why the thickness of these inner plates is not strictly significant on results, as it can be seen in figure III.22.

In the elastic-plastic range of section C2, vertical stress of concrete grows up to values of 80 MPa in some areas of the core [200% of the f_{ck}], and up to 100MPa in section C4 [that is, 250% of the f_{ck}]. The evolution of vertical stress in concrete is represented in the evolutionary sequence shown in figure VI.15, until point D⁶. Note that the maximum compressive strength of concrete takes place at strains of 0.005, a value which is notably higher than its analogous unconfined, 0.002; this is caused by the natural increment of ductility in concrete subjected to high hydrostatic states. As in case of unstiffened circular CFT sections, confinement effect grows up concentrically from the centroid: while in case of section C4 the confined area remains focused on central area of the core, in case of C2 this area becomes more lengthened, parallelly to the stiffening plate.

⁶ corresponding approximately to the peak of load.

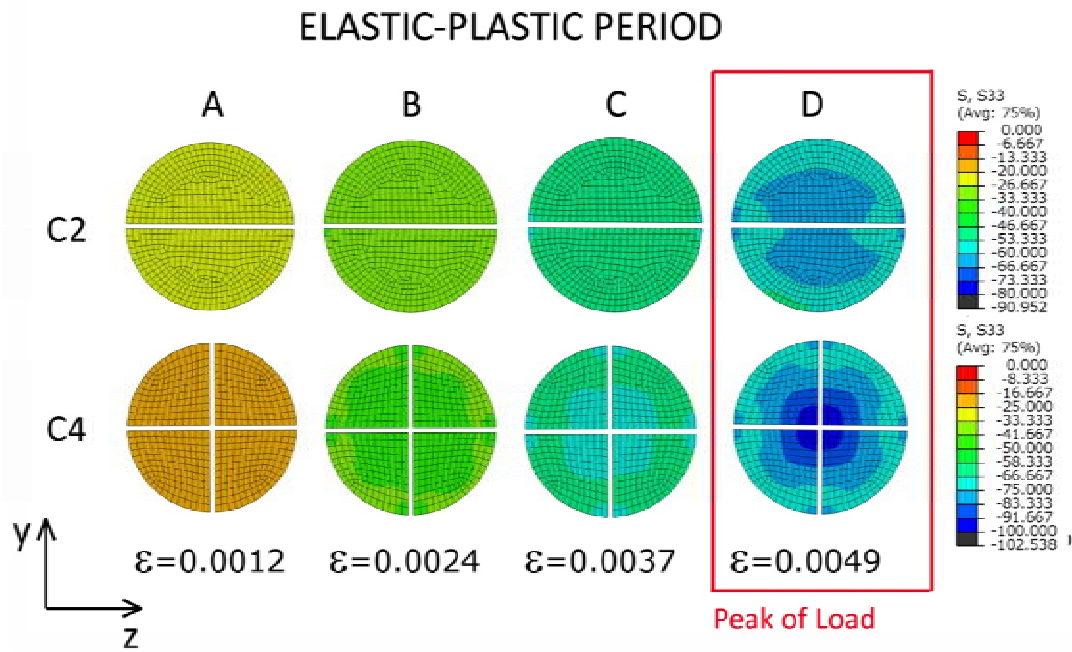


Fig. VI.15 Evolutionary sequence of vertical stress until the peak of load in sections C2 and C4.

Different stress ranges have been considered to represent the confined areas of the core.

Needless to say that all vertical stresses well above the maximum uniaxial compressive strength of concrete [40MPa] are a result of the hydrostatic pressure in those specific areas. In figure VI.16 we can see how circular sections become triaxially compressed in the whole area of the core, although some specific areas become more stressed than others. Stress in the [z] and [y] axes reflect the influence of the stiffening plates on the core: while in section C2 [with one single plate] lateral stress varies from 5 to 10 MPa [similar to the case of circular unstiffened tubes], in section C4 this lateral pressure is increased until values of 15-20 MPa.

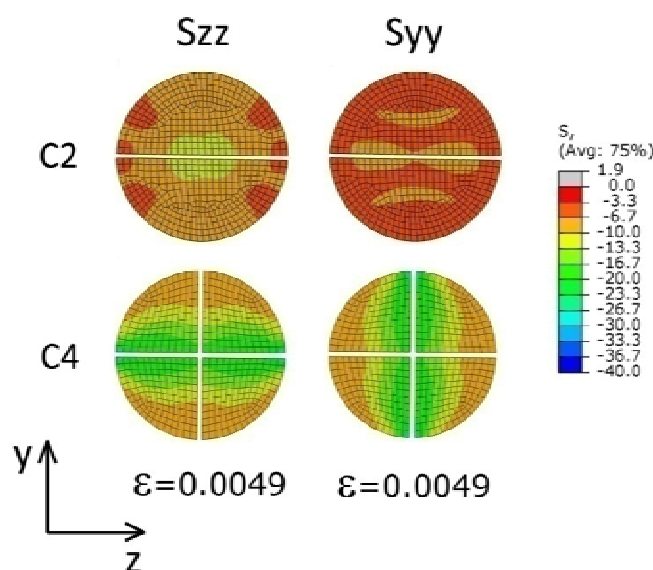


Fig. VI.16 Stresses in the [z] and [y] axes at the peak of load. Sections C2 and C4.
Transversal stresses define with accuracy the shape of confinement in concrete core.

In the following sequence of figure VI.17, the stress state in the [y] and [z] axes has been idealized by using the results obtained in the FE analysis, and it has been superimposed on the cross-sectional plane in order to detect those more confined areas. The result is the diagram shown on the right column, with some areas of the core slightly confined and other areas much more confined. Note that the obtained results match considerably with the distribution of vertical stress in the core at point D of figure VI.15. Thus, the superimposition of transversal stresses in the two axes determines the percentage of confined area in concrete core.

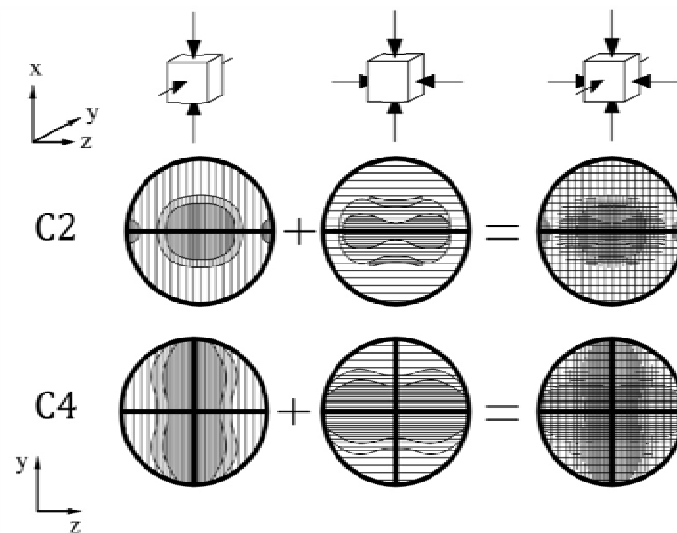


Fig. VI.17 Idealized pattern of stress distribution in the core, sections C2 and C4.

The combination of compressive stresses in the [y] and [z] axes defines the confined areas of the core accurately.

Beyond the peak of load [point D in diagrams of figures VI.11 and VI.12], the concrete core continues the escalation of vertical stress up to the ultimate load in point G of the mentioned diagrams. During the hardening period, the tube persists confining the concrete filling and, as a consequence, vertical stress of the concrete core keeps on still growing well above the values reached at point D [see Fig. VI.15]. The evolutionary sequence of vertical stress in the core beyond the peak of load for sections C2 and C4 is represented in the two sequences shown below.

Note the difference between introducing one or two stiffening plates in the core, especially during the plastic hardening period. While confinement is sensibly higher in section C2 than in a theoretical homologous unstiffened section, this effect is really more significant in section C4. Hydrostatic pressure on the core allows reaching so high values in section C4 that compressive strengths of concrete achieve extraordinary values up to 100 MPa at most part of the concrete area [see Fig. VI.18].

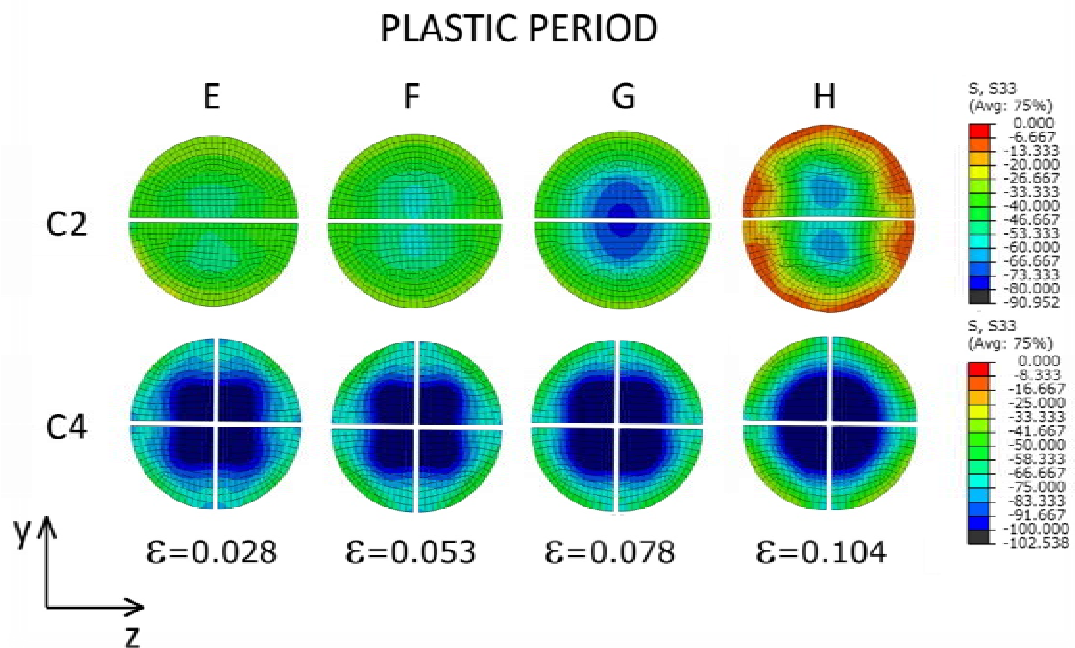


Fig. VI.18 Evolutionary sequence of vertical stress beyond the peak of load in sections C2 and C4.

Different stress ranges have been considered for section C2 and C4.

6.2.4 Damage evolutionary analysis of concrete.

It has been explained before that a tensional analysis is not enough to describe the compressive response of CFT sections [see Chapter V]. Concrete confined by a tube is capable of resisting much higher stresses than in case of not being confined. Cohesive materials like concrete subjected to large deformation axial loading suffer an irreversible damage process as a consequence of the appearance of crushing in the cement paste. However, while this process is going on further, concrete is still capable of resisting surprising compressive loads thanks to be contained in a rigid recipient. At these advanced stages of axial deformation, concrete is much closer to behave as a filling of sand than as a compact cohesive material.

Damage evolutionary ratio $[d]$ depends on the confinement provided by the tube and on the axial deformation rate. This leads to different evolutionary curves of damage-strain, depending basically on the stiffness of the tube; thus, the D/t ratio becomes crucial in order to determine the velocity of this process. Note how concrete of sections C2e and C4e [with plates of 5mm thick] is quickly damaged, while sections C2b and C4b [with plates of 10 mm thick] clearly delay this phenomenon. Besides, residual stress of concrete is always higher in those cases corresponding to thicker tubes.

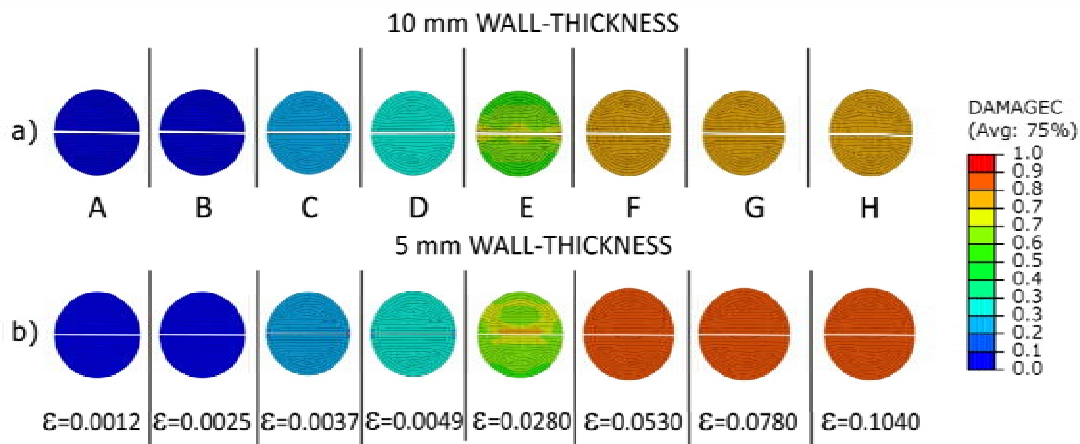


Fig. VI.19 Evolutionary sequence of compressive damage ratio in concrete core, section C2.
a) section C2b [10 mm wall-thickness] b) section C2e [5 mm wall-thickness]

The more rigid is the tube, more delayed is the damage process. This phenomenon can be clearly observed in figure VI.20, where the evolution of damage in section C4 is shown. In sections with plates of 5 mm wall-thickness [belonging to the second group], there are no significant differences between introducing one or two stiffening plates. The tube is quite deformable in both cases, so that concrete is damaged by following a similar pattern. Contrarily, in sections with 10 mm tube wall-thickness, the introduction of two stiffening plates instead of only one has a positive influence on the evolution of damage [see sequence a) of figure VI.20].

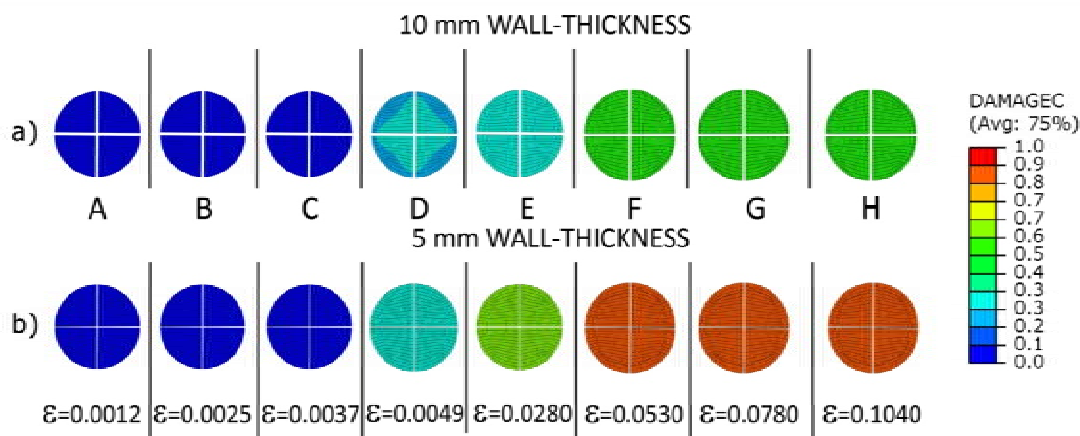


Fig. VI.20 Evolutionary sequence of compressive damage ratio in concrete core, section C4.
a) section C4b [10 mm wall-thickness] b) section C4e [5 mm wall-thickness]

The damage process is intimately related with the dissipated energy by the core. The extraordinary ductility shown by concrete-filled tube sections generally derives from the intrinsic capacity of concrete of being damaged through crushing. The damage of concrete stiffness is directly related with energy absorption; if this damage does not go hand in hand with a significant load decrement [as in most cases of thick-walled CFT sections] this conjunction becomes really useful for columns subjected to severe dynamic loading. This is the reason why concrete-filled tubes are been increasingly used for tall structures in seismic areas.

The evolution of compressive damage starts in the centroid of the section, spreading quickly to the perimeter. Crushing of concrete begins first in those areas where the core is more confined, being generalized progressively to the whole section as the axial strain increases [see figure VI.21].

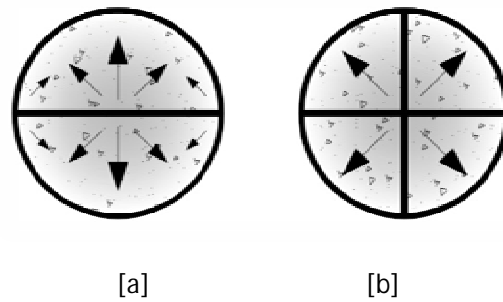


Fig. VI.21 Progress of compressive damage in reticulated circular CFT sections.
a) Section C2 b) Section C4

By analyzing the relation between vertical stresses in concrete and the damage dissipation energy, we can conclude that the most important part of this crushing effect occurs beyond point “a” in figure VI.22. The evolutionary damage process starts at an approximate value of stress of $0.5 f_{ck}$, up to its maximum compressive confined strength [coinciding with point a]; from this point, the process goes faster up to the ending of the softening period. Figure VI.22 shows the evolution of damage dissipation energy compared with the progress vertical stress of concrete, for sections C2b and C2e with different D/t ratios.

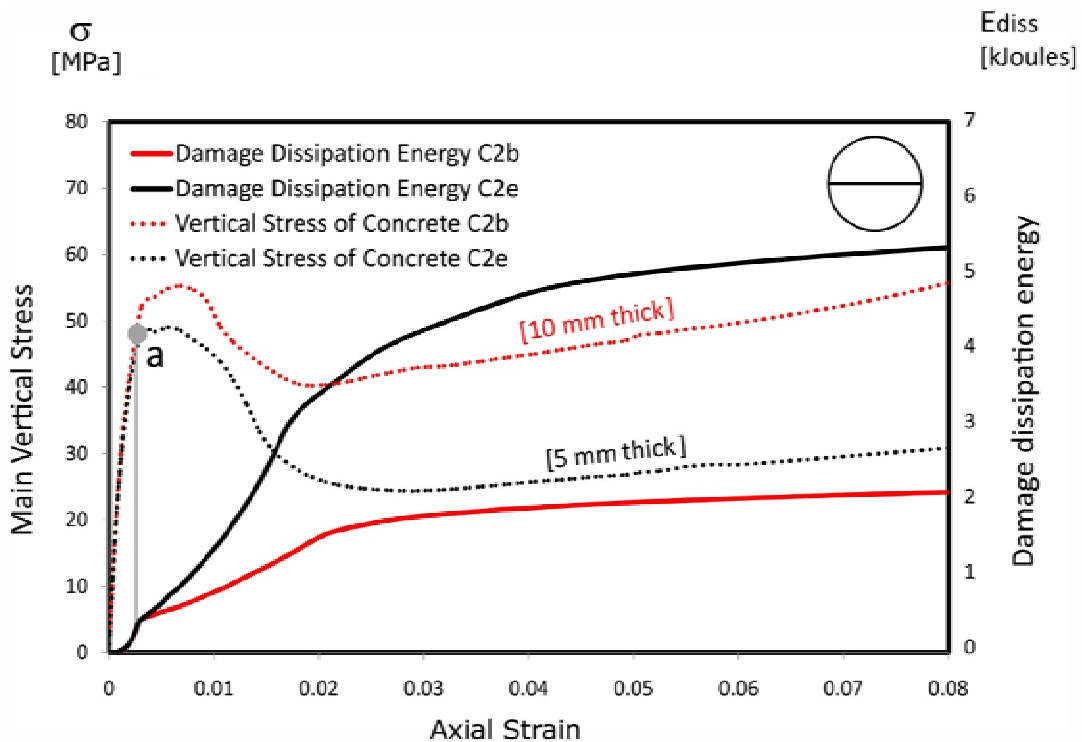


Fig. VI.22 Damage dissipation energy in section C2.
Red curves belong to section C2b [10 mm thick] and black curves to C2e [5 mm thick]

From the previous figure, it can be clearly seen how tubes with high D/t ratios dissipate more energy through damage than their homologous thicker sections. It has been commented before that hydrostatic pressure on the core clearly delays the damage process (Mirmiran, et al., 2000); therefore, this is the reason why sections with low D/t ratios show less degradation of concrete and smoother softening branches. In figure VI.22, the evolution of damage ratio in concrete [d] for sections C2b and C2e is shown. Note how the damage ratio for both specimens is about 0.2 at the peak of load [point B in figure VI.23]; this means that to reach the maximum load-bearing capacity

of the composite section, it is necessary that the core is partially damaged. From point B to C, the growth of the damage ratio is clearly exponential, especially for section C2e [with plates of 5 mm wall-thickness].

In the illustrative sequence at the top on the right of figure VI.23, it is represented the evolution of damage through crushing of concrete. Until point A, the material is completely undamaged and behaves almost elastic; from points A to B, there is a first damage process owing to volumetric expansion of concrete, and beyond point B, damage is severely enhanced owing to the softening. Straight lines superimposed to the stress-strain curves represent the evolution of the damaged proportional modulus at each singular point and the contiguous attached numbers correspond to the approximate compressive damage ratios.

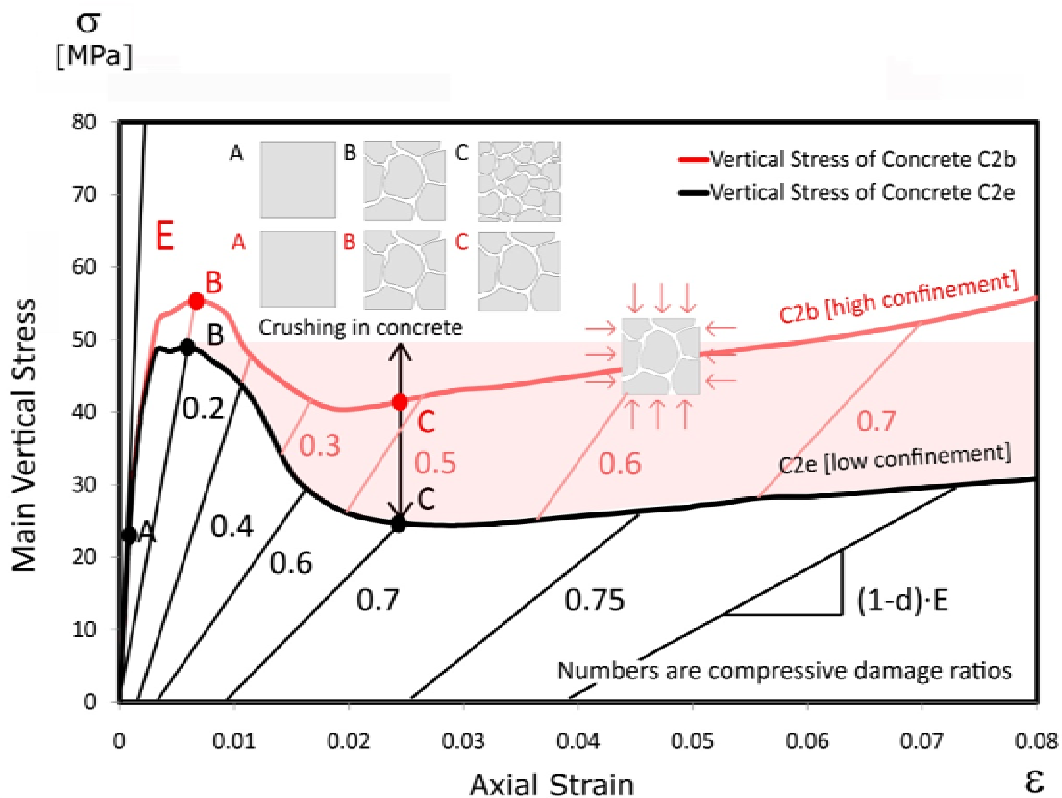


Fig. VI.23 Evolution of compressive damage ratio and stress-strain curves for concrete.

The red curve belongs to section C2b [10 mm wall-thickness]
and the black curve to section C2e [5 mm wall-thickness]

6.2.5 Analysis of contact pressure.

The distribution of contact pressure on the core constitutes a clear radiography of the distribution of confinement effect, as the tube provides lateral pressure to the core through the interface between both components. In figure VI.24a) we can see how lateral pressure is distributed on section C2 and in figure VI.24b), the same distribution on the core of section C4. Note how lateral pressure is completely uniform on concrete core owing to the effect of a circular geometry, especially in section C2. In addition, it is curious to see the restriction to buckling of stiffening plates by using the negative of the stress distribution on concrete core [see figure VI.24 a)]; the shape of the distribution of normal pressure on the embedded plate in section C2 clearly represents the

restriction provided by concrete filling. Less explicit is the case of section C4, where these plates are not directly subjected to second-order effects.

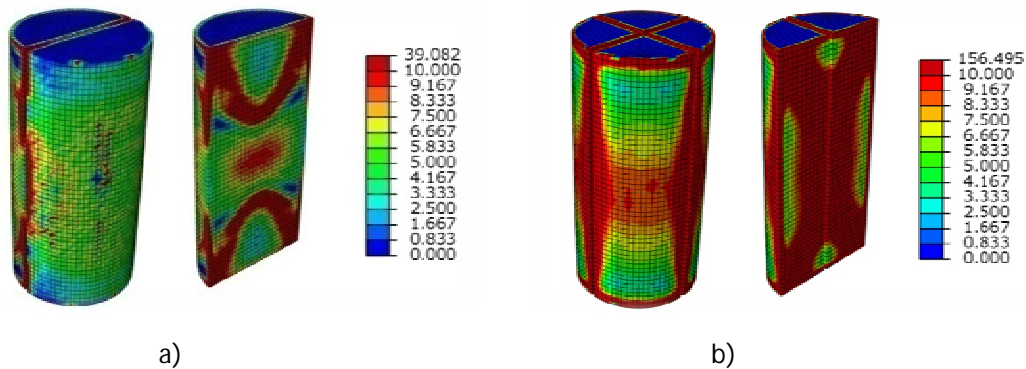


Fig. VI.24 Distribution of contact pressure on the core in sections C2 and C4.

In case of section C4, the distribution of contact pressure on concrete tends to be focused on the four intersection points. This fact implies a clear variation of the tensional path, from circular to cruciform, so that confinement effect comes more from the intersection of the two embedded plates than from the effectiveness of a circular geometry. In figure IV.24b, the highest contact stresses are located in the nearby of these stiffening plates.

6.3 Large deformation axial loading behavior of square-shaped reticulated CFT sections.

Following similar criteria used for circular sections in Section 6.2, and according to the assumptions established for the analysis in Section 6.1, three different reticulated square-shaped typologies have been also proposed and studied in this investigation. They are based on the principle of converting a square-shaped section into a reticulated-shaped geometry, made of embedded plates restricted to buckling thanks to the concrete filling. These three reticulated typologies have been named as R2, R4 and R9, of two, four and nine alveoli, as it has been explained in Section 6.1.

Similar to the case of circular sections, these three different typologies have been varied for comparison purpose, by changing their geometrical and material properties. First parameter which has been varied is the thickness of the outer tube, according to tables VI.3, VI.4 and VI.5. A total of eighteen specimens [six different cases per typology] has been divided into two groups, depending on the B/t ratio: the first group with plates of 10 mm wall-thickness [a value which corresponds to a ratio of $B/t=20$ for R4 and R9, and $B/t=40$ for R2] and the second group with plates of 5 mm wall-thickness [$B/t=40$ for R4 and R9, and $B/t=80$ for R2]. Parameter B in this case is assumed as the wider dimension of an individual loading cell [400 mm for section R2 and 200 mm for the rest], and it is known as B_{cell} . On the contrary, stiffening plates have been always considered 1.20 times thicker than the outer [$t_{inn}=12\text{mm}$ for the first group, and $t_{inn}=6\text{mm}$ for the second one], as it has been previously commented.

6.3.1 Geometrical features of the analysis.

According to Chapter IV, the sections have been modeled entire although they were all symmetrical. Besides, it has been assumed an important size of the samples in order to guarantee the maximum accuracy of results as possible; thus, a height of two times the width of the specimens has been chosen, like for the case of circular tubes. This way, in sections R2 and R4 -composed by two and

four alveoli, respectively- specimens are 800 mm height according to a minimal width of the alveoli of 200 mm. By following this criterion, section R9 is 1200 mm height due to the fact of being composed by three rows of alveoli, instead of two.

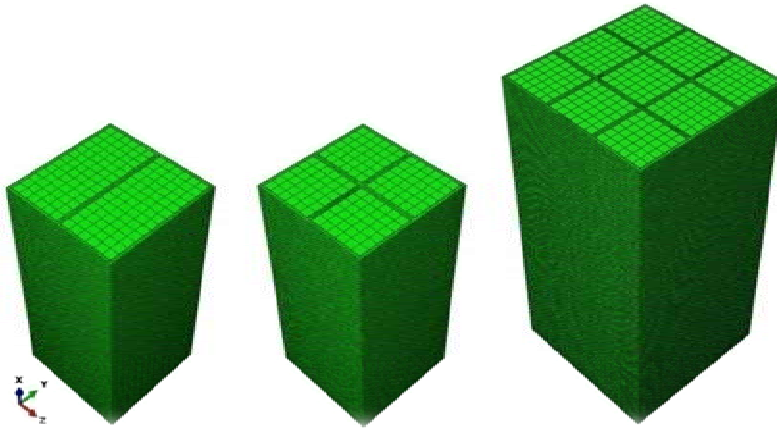


Fig. VI.25 Finite Element Mesh used for square-shaped specimens.

The mesh size coincides with the conditions established in Chapter V.

All other conditions coincide with the criteria considered for circular sections in Section 6.2 [boundary conditions, way of loading, etc], and derived from Chapter IV.

6.3.2 General compressive response and ductility.

Sections belonging to the first group [those with thick plates] do not show a significant descending branch in the softening period of concrete, except for the case of section R2. Sections R4 and R9 with plates of 10 mm wall-thickness describe a wide horizontal yield plateau [see Fig. VI.26], while section R2 suffers a slight load decrement owing to the deformability of the unstiffened plate. Thanks to the elevated B/t ratio of the first sectional group, a load-strain curve without important discontinuities is fully guaranteed. Confinement effect on concrete is almost constant after the peak of load, by keeping the load also invariable and delaying the process of damage by means of hydrostatic pressure. More details of concrete behavior and its damage process in these sections will be explained in Section 6.3.3.

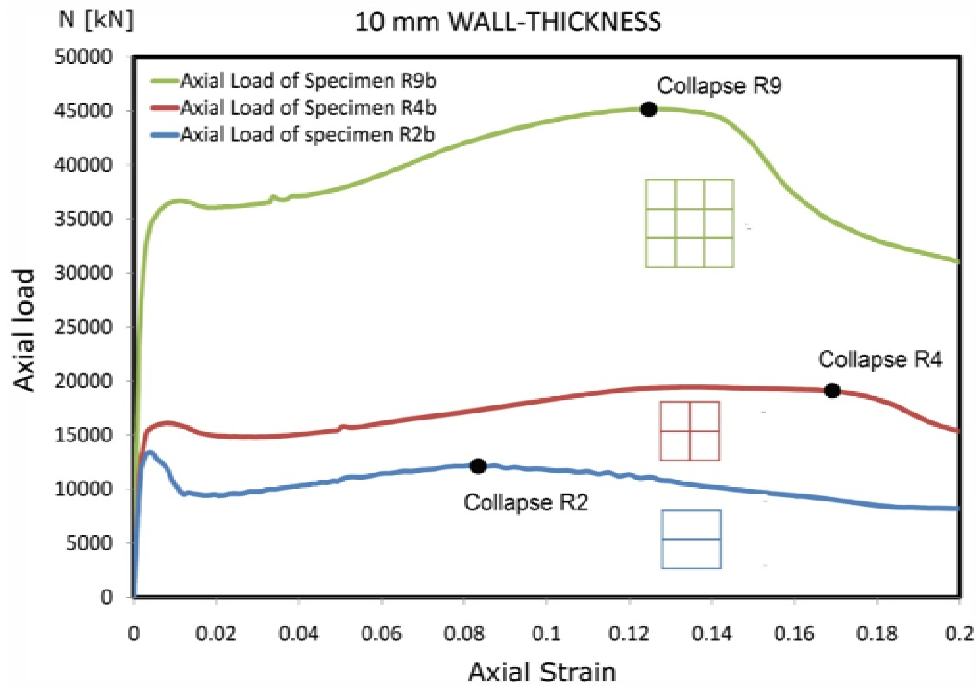


Fig. VI.26 General axial load-strain curves obtained from the FE analysis. Sections R2, R4 and R9, with 10 mm wall-thickness [$B/t=20$ for R4,R9 and $B/t=40$ for R2].

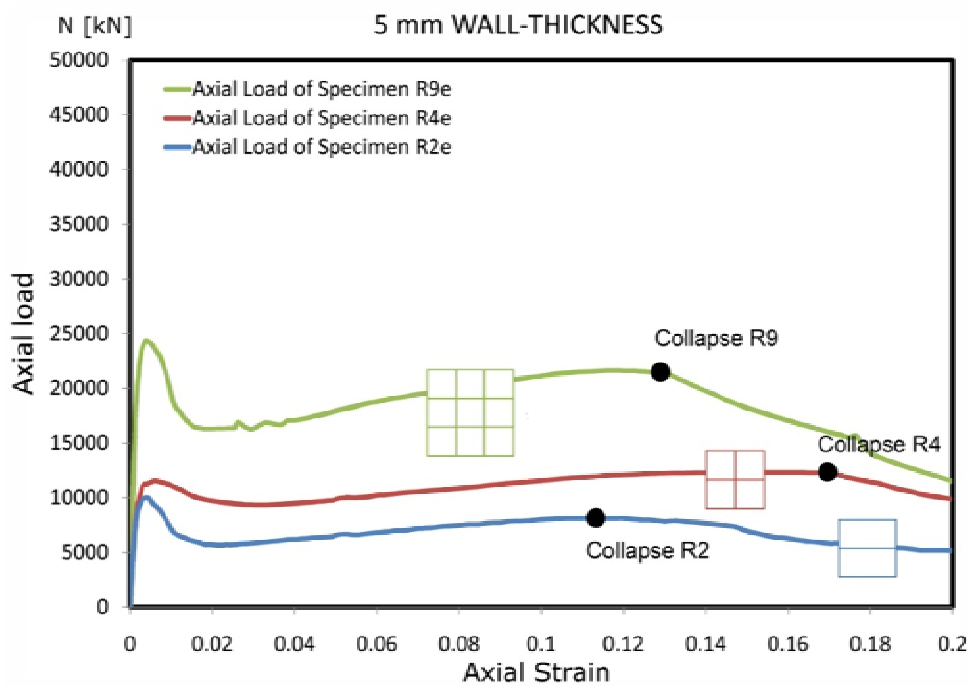


Fig. VI.27 General axial load-strain curves obtained from the FE analysis. Sections R2, R4 and R9, with 5 mm wall-thickness [$B/t=40$ for R4,R9 and $B/t=80$ for R2]

The most important difference between the three square-shaped typologies –apart from an obvious difference in the magnitude of the peak of load- is the plastic hardening behavior. While the three sections collapse between strains of 0.08 and 0.12, the hardening slope is much steeper in section

R9 than in the other two. This phenomenon is justified by the percentage of steel respect to the total area and its ability to confine the concrete filling; this fact also means that the mode of failure is really different from one to other. While sections R2 and R4 collapse softly, the failure of R9 is much sharper after reaching the ultimate value of plastic load. In the same way, also residual stress is affected by the shape of the outer tube: the higher is the ultimate stress before the collapse, lower is the residual stress.

Referring now to the second group [sections with plates of 5 mm wall-thickness], all the specimens show significant softening periods independently of the number of stiffening plates, since the deformability of the tubes is normally much more important. The percentage of load decrement is proportional to the rigidity of the tube. Nevertheless, there is a big difference between the compressive response of sections R4/R9 and R2, owing to the flexibility of the tube [with only one stiffening plate]. This fact reduces significantly the ductility of the composite section. It can be clearly seen in figure VI.27 how the energy of fracture is much lower in section R2 than in the other two typologies, by collapsing at values of strain about 0.11.

Comparing the diagrams corresponding to figures VI.26 and VI.27, it can be seen that the elastic-plastic confinement period is more important in those sections with lower B/t ratios, by reaching higher stresses in concrete and also higher load responses. While concrete starts softening at approximate strain values between 0.006 and 0.01 in case of 10 mm thick sections, this process takes place at strains between 0.003 and 0.005 in thinner tubes. Needless to say that all these typologies show a significant rate of ductility, by collapsing at advanced percentages of deformation [in most cases, at strains of 0.10].

Differences in the compressive response between typologies and B/t ratios can be explained by simplifying the curves into equivalent proportional modules of the composite section, by following the same procedure as used in Section 6.2.2. These proportional modules can be easily calculated and compared for each typology, according to expression (6.1):

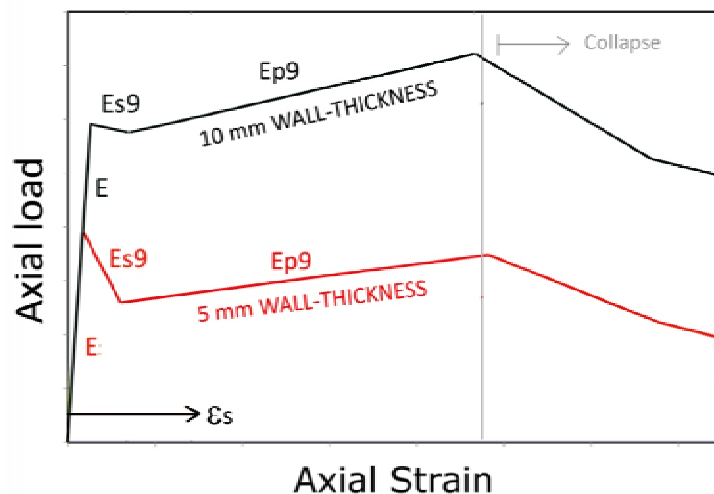


Fig. VI.28 Idealization of the load-strain curves for square-shaped sections.
Proportional modules of sections with 10 mm wall-thickness [in black]
and sections with 5 mm wall-thickness [in red]

And obtained values for each typology are the following:

Table VI.10 Composite plastic modules for section R2.

Section R2	E2	Es2	Ep2
$t_{out}=10\text{mm}$	28100	-1680	224
$t_{out}=5\text{mm}$	19790	-1660	95

* All values expressed in N/mm².

Table VI.11 Composite plastic modules for section R4.

Section R4	E4	Es4	Ep4
$t_{out}=10\text{mm}$	15170	-625	139
$t_{out}=5\text{mm}$	15000	-1040	121

* All values expressed in N/mm².

Table VI.12 Composite plastic modules for sections R9.

Section R9	E9	Es9	Ep9
$t_{out}=10\text{mm}$	10300	-378	210
$t_{out}=5\text{mm}$	13600	-1603	145

* All values expressed in N/mm².

This way, the load decrement during the softening period for each typology can be quantified. For specimens belonging to the first group [with plates of $t_{out}=10\text{mm}$], the influence of geometry on their stiffness is evident, as the proportional modules quickly decrease from R9 to R2. By the contrary, in sections of the second group, the proportion of the descending branch is quite similar for all typologies [between 1040 and 1660 N/mm²]; this similarity is caused by the low rigidity of the tubes, independently of geometry. The observed difference in the softening period between different typologies can be also observed in the mode of failure, by analyzing the values of $[Ec]$. The more stiffened are the tubes, sharper is their collapse; for instance, in case of section R9, with a descending branch after the failure of $E_c=-370$, while the same value for R2 is -10.

It is evident that all these sections show a significant rate of ductility, and no doubt that the shape and the rigidity of the stiffening plates play a decisive role in the determination of its magnitude. Ultimate axial deformations between 0.11 and 0.15 represent a significant gain in ductility respect to their equivalent unstiffened square sections⁷. This postponement of collapse implies an important absorption of energy until the failure, by converting these sections in a really suitable typology for structures subjected to severe dynamic loading.

6.3.3 Tensional behavior of components.

Steel has also a determining role in the global compressive response of square-shaped reticulated sections, even more than in case of circular tubes. Main difference between behaviors lies in the influence of the deformability of the plates on confinement effect. Lateral deformation of plates in

⁷ See figure V.1 in the previous Chapter.

these sections may be quite notorious, depending directly on their buckling length; as more stiffened is a plate, more confinement can provide to the core.

In the set of analyzed specimens, local buckling only appears in the elastic range in sections R2d, R2e and R2f. The high B/t ratio of the wider and unstiffened side of the tube involves the appearance of local buckling in points B and C of the evolutionary sequence b) of figure VI.29. These points coincide with the points shown in figures VI.34 and VI.35.

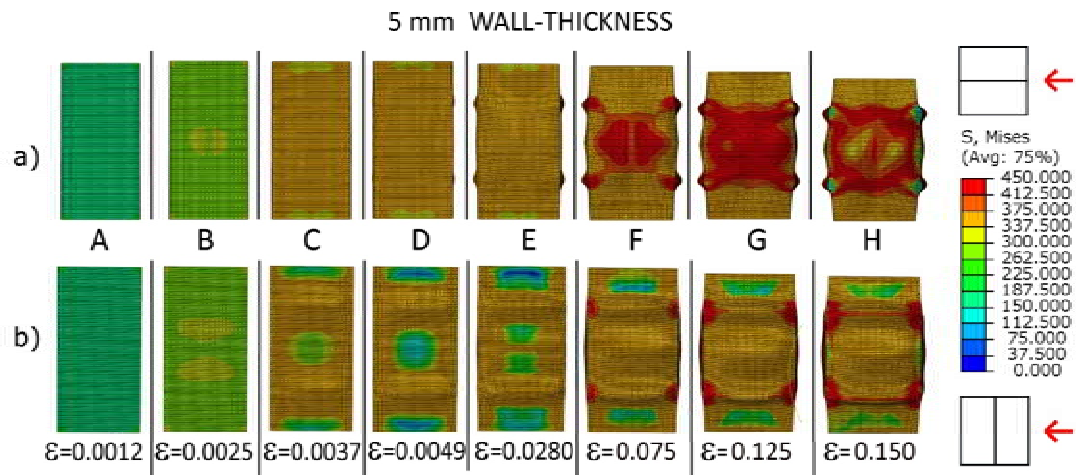


Fig. VI.29 Evolutionary sequence of von Mises stress in section R2e [5 mm wall-thickness].
Case a) refers to the view parallel to the inner plate and case b) refers to that perpendicular.

The deformed shape of section R2e follows accurately the pattern predicted by the Theory of Elastic Stability⁸, owing to the elastic local buckling of the plates. As it is derived from Section 3.3.2.1, the value of the half wavelength of the deformed plates [restricted against rotation in the two unloaded edges and clamped in the two loaded edges] coincides exactly with the value of the cross-sectional width. In figure VI.30, the tensional distribution of von Mises in section R2 with plates 5 mm thick [case a)], and 10 mm thick [case b)] is compared.

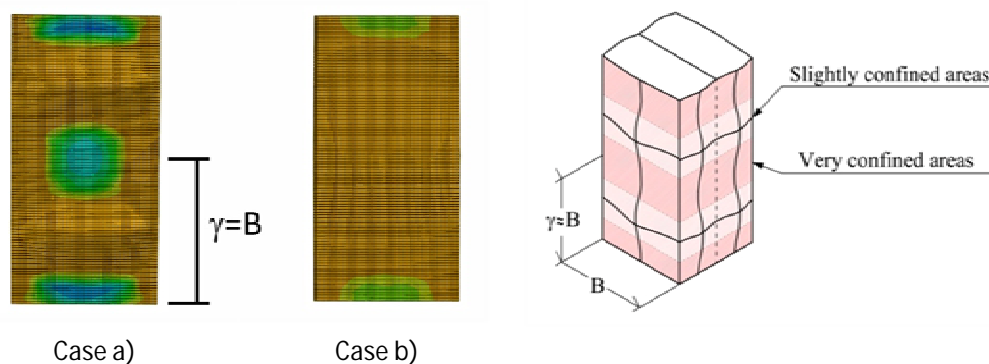


Fig. VI.30 Comparison between the deformed shapes of sections R2e and R2b.
Case a) refers to section R2e, case b) refers to section R2b.
Tensional distribution of von Mises at the peak of load [point D in figure VI.34]

⁸ (Timoshenko, et al., 1961)

Note how important is the plate thickness and the number of stiffening plates. While section R2e buckles in the elastic range, its homologous section with two inner plates instead of one, R4e, is not affected by this phenomenon thanks to the rigidity of the reduced alveoli [see sequence b) in figure VI.31]. Deformation coming from local buckling has a clear effect on the confinement effect of the core. The mode of failure of section R2 is quite different from the failure experimented by sections R4 and R9. The fact of disposing a set of stiffening plates symmetrically respect to the centroid, by forming a perfect grid of independent alveoli, makes that square-shaped sections do behave in a similar way to circular sections. If we compare the mode of failure of section R4 in the sequence b) of figure VI.31, with that of sections C2 and C4, it is obvious that there is so much in common.

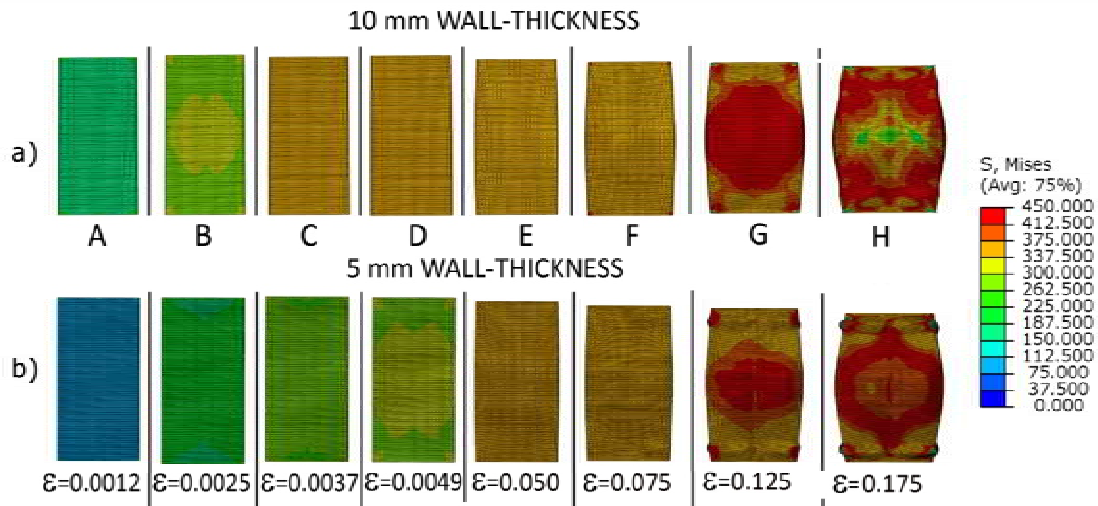


Fig. VI.31 Evolutionary sequence of von Mises stress in specimen R4.

Case a) refers to section R4b [10 mm thick], case b) refers to section R4e [5 mm thick].

Main difference lies in the origin of the collapse. While in section R2, the failure of steel comes from an excessive curvature of the widest plate, in sections R4 and R9 the initiation of the collapse goes hand in hand with plastic local buckling, according to the shape in *elephant foot*. In these cases, local buckling goes always accompanied by an excessive stress state of the plates in the middle height of the specimens, caused by the volumetric expansion of concrete core. The failure takes place by following exactly the same procedure as in case of circular sections.

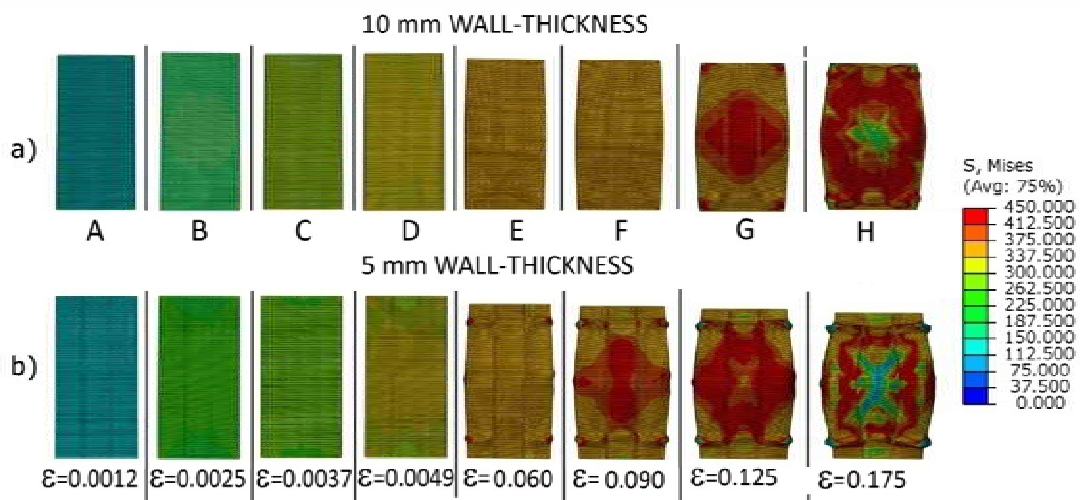


Fig. VI.32 Evolutionary sequence of von Mises stress in specimen R9.

Case a) refers to section R9b [10 mm thick], case b) refers to section R9e [5 mm thick].

Comparing the ductility shown by sections R4 and R9, we can detect a surprising difference in their behavior. Curiously, the collapse of section R4 appears much later than that of section R9. Although the confinement effect of central alveoli is higher and the hardening period is even more decisive in section R9 than in section R4, first typology collapses earlier and much brusquely than the latter. This phenomenon is intimately related with the compressive behavior of stiffening plates: while these plates are completely restricted to buckling in sections R2 and R4, in section R9 they become deformed during the plastic range, a fact that anticipates the collapse.

The eccentricity of the stiffening plates respect to the centroid plays a decisive role in determining the ductility of these sections. Those plates crossing the centroid do not suffer from buckling effects, either during the plastic period, since the expansion of concrete always occurs outwards; contrarily, those plates which are separated respect to the centroid tend to bend as a consequence of the volumetric expansion of concrete. This effect goes against the growth in size of reticulated sections, although as more reticulated is the section, more confined is the filling. Note from figure VI.33 how vertical stress in central plates of section R9e is lower than the homologous stress in section R4e, owing to lateral deformation.

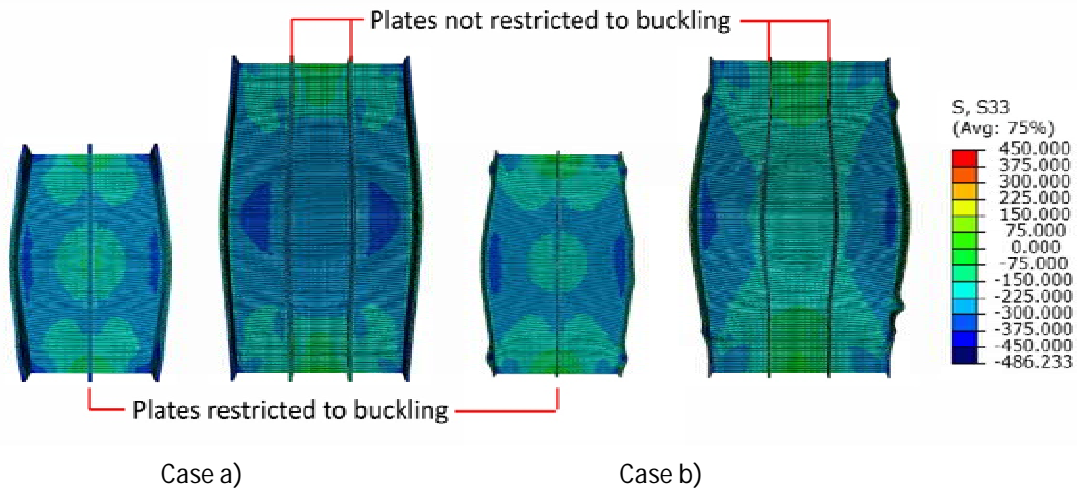


Fig. VI.33 Distribution of vertical stress in the stiffening plate [point F in diagrams] specimens R4 and R9.

Case a) refers to specimens R4b and R9b [with plates of 10 mm thick],

Case b) refers to specimens R4e and R9e [with plates of 5 mm thick].

Comparing vertical stress of stiffening plates in specimen R2 with that of the plates of specimens R4 and R9, we can conclude that the fact of having two, three or four shared edges with transversal plates does not lead necessarily to significant differences in the stress distribution. As it is derived from figure VI.33, the less stressed areas of stiffening plates coincide basically with their central parts.

In the following two diagrams, the evolution of vertical stress in both components is compared. The two materials are intimately related as in case of circular CFT sections, and each one of the five previously described phases for steel can be also detected here, with some specific particularities. It is worth to note that steel does not reach its yield limit stress [355MPa] in figures VI.34 and VI.35, since these diagrams reflect only the vertical stress component. Yielding of steel occurs when the

combined von Mises stress reaches the maximum value of 355MPa, owing to the combination of vertical and transversal⁹ components.

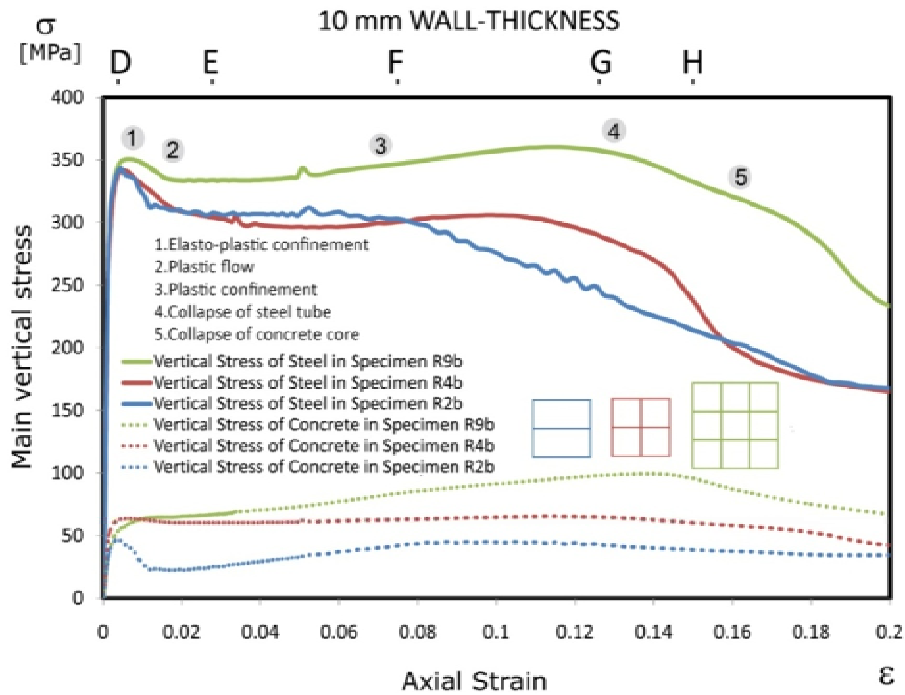


Fig. VI.34 Averaged vertical stress of components in reticulated square-shaped sections.
Diagrams corresponding to specimens composed of plates of 10 mm wall-thickness.

Note that the maximum value of vertical stress reached by the curve in specimen R2e is about 315MPa, owing to local buckling effects in the elastic range. In the first group, corresponding to sections with low B/t ratios, there is a clear difference between the behavior of specimens R4/R9 and the behavior of section R2 during the yield plateau. On the contrary, all those sections with thin plates show a significant descending branch, starting from the maximum compressive load at point 1 of figure VI.35.

Sections of the first group are not subjected to local buckling in the elastic range; however, buckling of the plates in the plastic range always precedes their collapse. The initiation of this phenomenon is clearly reflected by point 4 of the curves shown in figure VI.35, where second-order effects accelerate the collapse of the section. After failing the steel of the tube, the load is progressively transferred to the core; at this stage of loading, the damaged concrete is not capable of resisting this transference of load, and finally it goes also quickly to the collapse.

⁹ In circular tubes, that component is known as hoop stress.

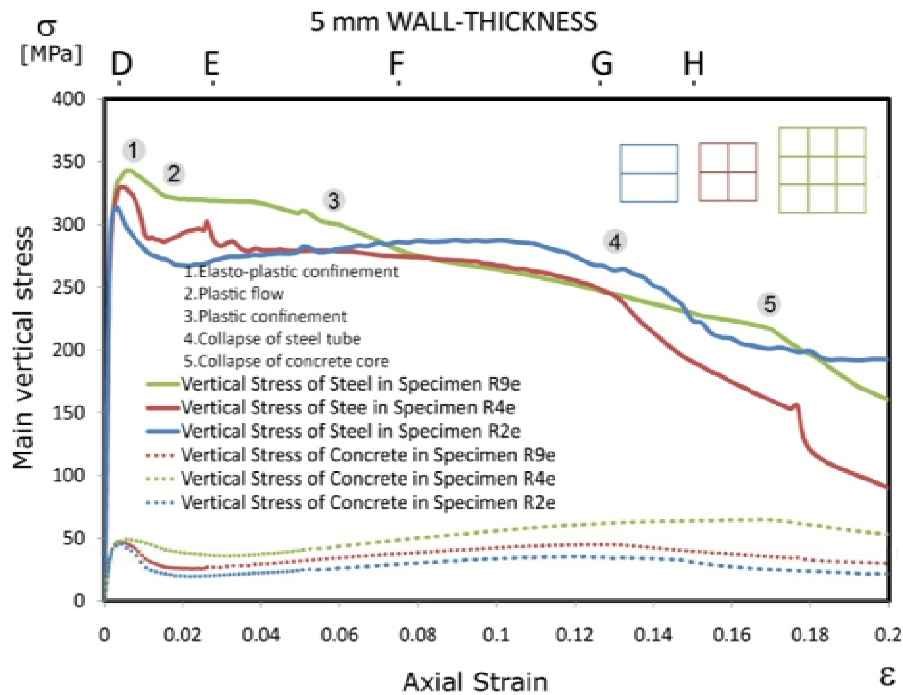


Fig. VI.35 Averaged vertical stress of components, square-shaped specimens.
Diagrams corresponding to those specimens composed of plates of 5 mm wall-thickness.

The values of the maximum vertical stress reached by the components and obtained from the FE analysis are summarized in the tables shown below:

Table VI.13 Maximum vertical stress of steel

Section	a	b	c	d	e	f
f_{ck}	30	40	50	30	40	50
R2	342.93	342.99	344.62	325.89	325.92	330.03
R4	344.02	344.07	346.23	341.92	341.87	346.64
R9	344.42	348.98	348.00	343.96	344.20	345.77

* All values expressed in N/mm².

Table VI.14 Maximum vertical stress of confined concrete.

Section	a	b	c	d	e	f
f_{ck}	30	40	50	30	40	50
R2	37.59	46.33	54.47	37.94	46.86	54.50
R4	52.73	64.47	67.58	39.99	48.40	56.52
R9	56.38	65.31	70.04	44.85	49.84	59.44

* All values expressed in N/mm².

The influence of stiffening plates on confinement effect is evident, from results shown in Table VI.14. The increment of strength is more significant in those sections filled with low strength

concrete, such as 30MPa or 40MPa. This is the reason why the lowest confinement effect appears at the right and on the top of the previous table, and the highest at the left and on the bottom. Assuming that the geometry of the stiffening plates has a considerable influence on the confinement effect over the core, it is important to study which is the evolutionary loading process during the elastic-plastic period. Each proposed typology behaves really different from the other, in terms of distributing lateral stress.

The presence of stiffening elements reduces local buckling of the outer plates, by increasing simultaneously the confined area of the core. The evolutionary sequences of vertical stress in concrete core of figure VI.36 represent these different distributions accurately, according to the elastic-plastic period before yielding. Since area does not grow linearly, section R9 is much more efficient than R2 from the point of view of confinement. Vertical stress of concrete core in section R9 not only reaches higher values, but also it tends to cover most part of the core. The loading process is always the same for all typologies: confinement effect spreads from the centroid to the periphery uniformly, except for specimen R2.

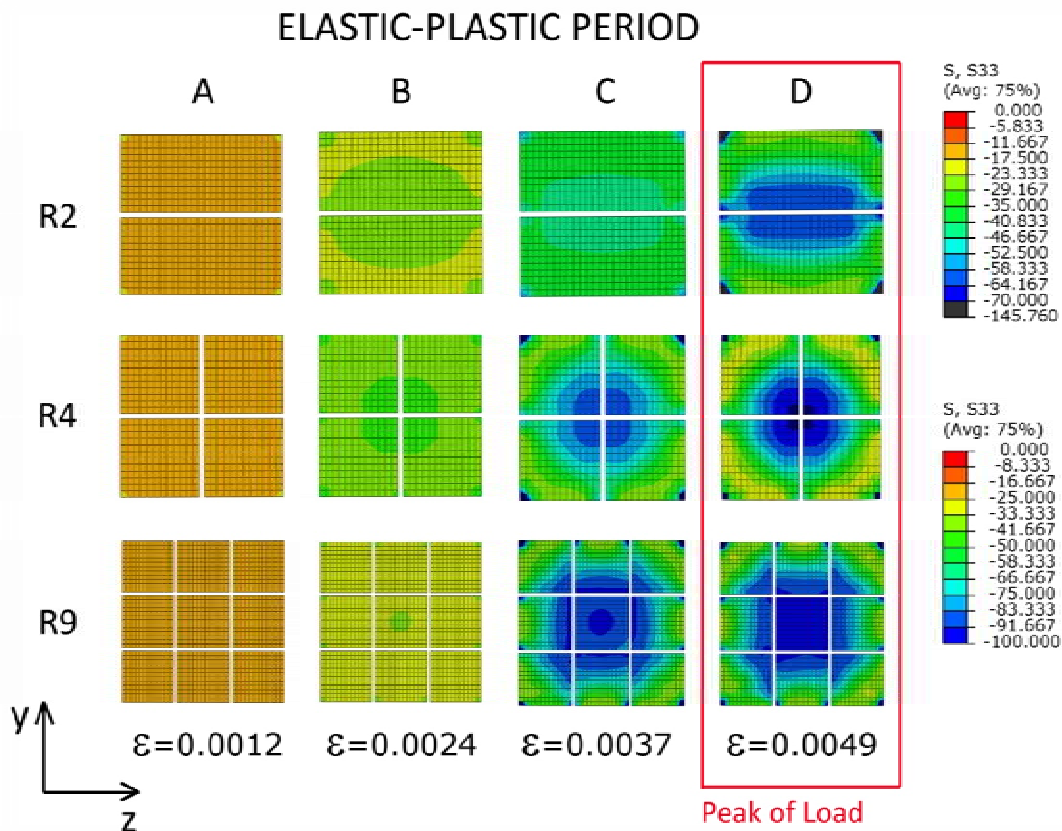


Fig. VI.36 Evolutionary sequence of vertical stress until the peak of load in specimens R2, R4 and R9.

Different tensional ranges have been considered in order to represent the confined areas. For points A,B,C and D, see figure VI.34.

The shape of confined areas in concrete is not casual. Accepting that all the section is compressed under pure vertical stresses, the blue-colored areas correspond to those parts where concrete is especially compressed in the three possible directions; the rest of the green-colored areas are biaxially compressed only, since there is one direction where stresses are really lower than in the other two. While in circular sections the core becomes uniformly confined as a consequence of hydrostatic pressure provided by the circular tube, the tensional distribution in square-shaped

sections is not uniform owing to geometry. Stresses in the [z] and the [y] axes are represented in figure VI.37:

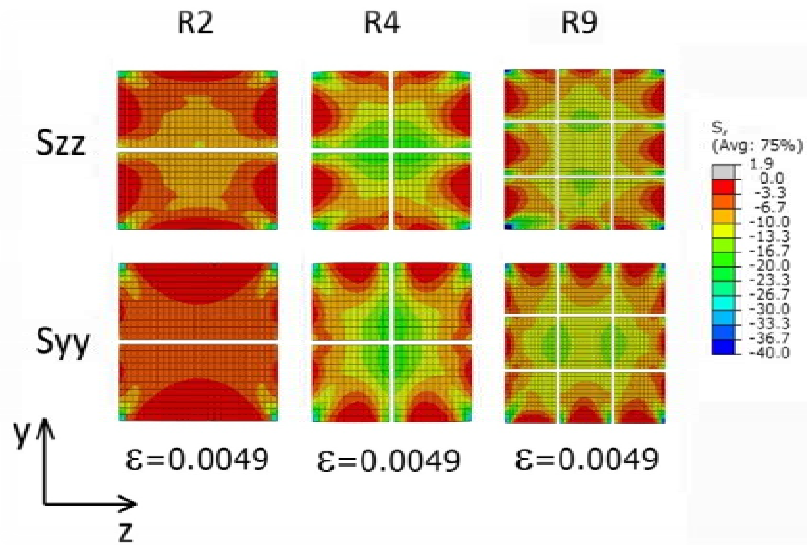


Fig. VI.37 Tensional distribution in the [z] and [y] axes in the peak of load, specimens R2, R4, R9.

Stress distribution in square-shaped sections is symmetrical respect to both axes.

Note that those areas of the core which show really elevated values of vertical stresses coincide with those areas coming from the superimposition of the compressive stresses in the [y] and [z] axes. Hydrostatic pressure appears always in central areas of the section, spreading progressively outwards; besides, the pattern of those confined areas can be usually assimilated to a rhomboid, owing to the rigidity provided by the introduced extra plates. Figures VI.38 and VI.39 show a theoretical idealization of the tensional distribution and the final pattern of confined areas in square-shaped sections:

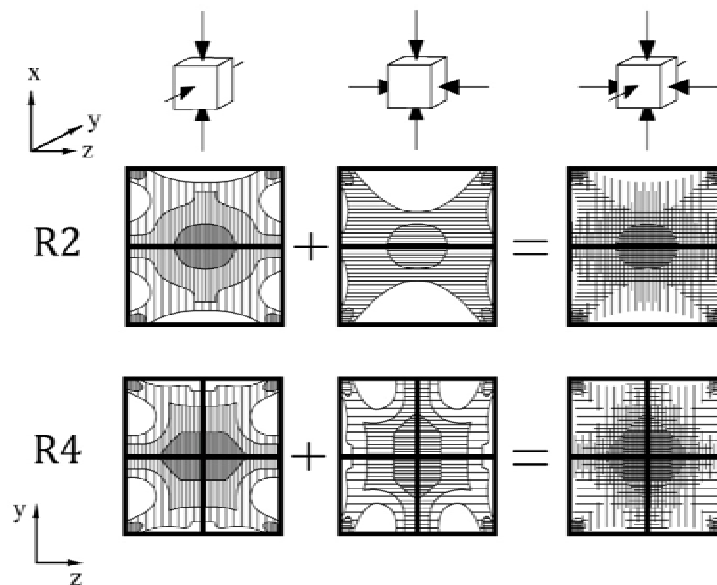


Fig. VI.38 Idealized tensional distribution in concrete core, sections R2 and R4.
Superimposition of stresses in the [z] and [y] axes, and the resulting confined areas.

The same simplification can be done for section R9:

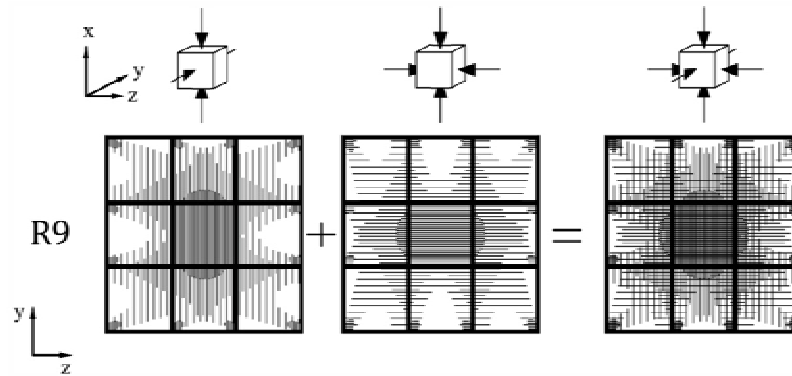


Fig. VI.39 Idealized tensional distribution in concrete core, section R9.

Superimposition of stresses in the [z] and [y] axes, and the resulting confined areas.

Densely grated zones are triaxially compressed [more or less intensively], while blank areas are only biaxially compressed. It is curious to see how the central alveolus of section R9 becomes severely and uniformly confined, independently of the thickness of the plates. This fact means that the whole concrete filling in this cell is capable of reaching much higher stresses than its maximum compressive strength.

The evolution of vertical stress in concrete beyond the peak of load is also different from one section to another. From point D in figure VI.36, the steel starts yielding; therefore, the load is transferred to the core until reaching the maximum compressive stress. From then, concrete of the core starts softening differently depending on the rigidity of the plates, and finishing this process at point E of Fig. VI.40. Note that the decrement of stress in section R2 is notably higher than in sections R4 or R9.

From point F of figure VI.40, concrete starts a second confinement period, caused by the plastic hardening of steel. Although concrete of the core is already damaged at this point, the fact of being laterally compressed by the tube implies the possibility of increasing its normal stress again. This is the reason why concrete reaches its maximum strength at vertical strains of approximately 8-12% [point G-H in Fig. VI.40], despite being completely crushed [see Section 5.3.3.2]. Beyond this period of "artificial" enhancement of concrete strength, steel fails by the weakest point –since it has reached its ultimate strength– and the entire load is transferred again to the core. The concrete, as cohesive material, breaks at 45° and the process finishes with the collapse of the section. After failure, only residual stress left thanks to the condition of being contained by a tubular section.

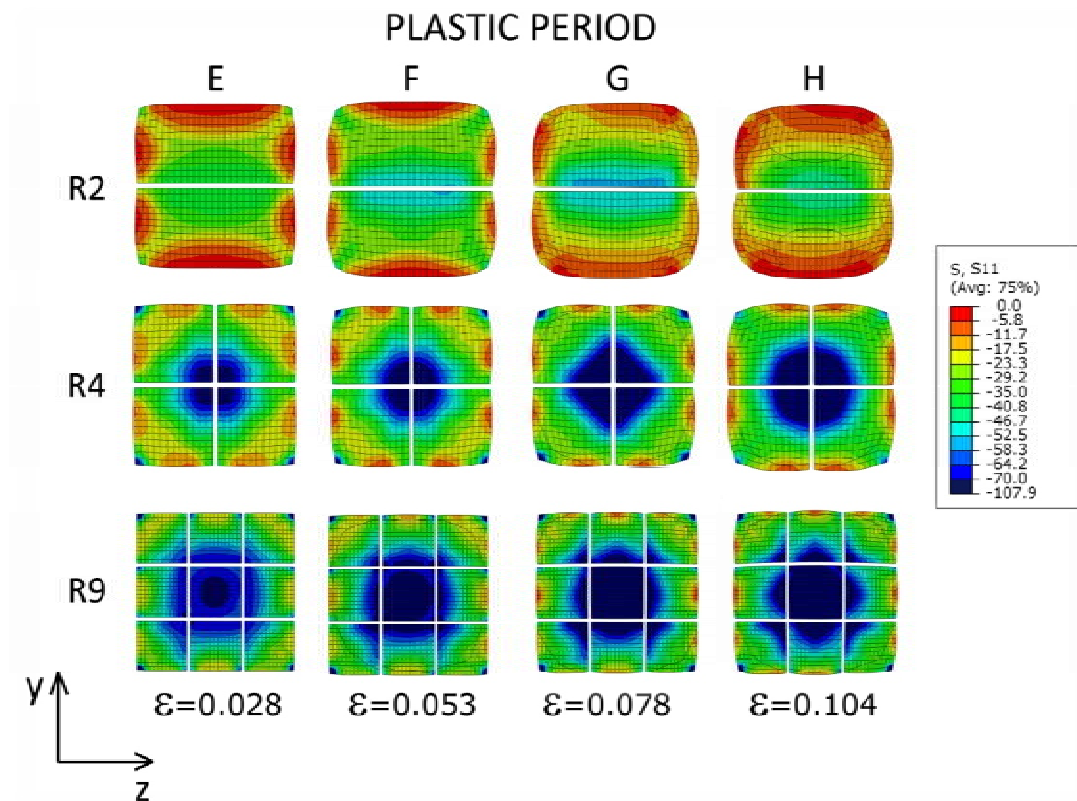


Fig. VI.40 Evolutionary sequence of vertical stress beyond the peak of load in specimens R2, R4 and R9.

The same tensional range has been considered in order to represent the confined areas.
For points E,F,G and H, see figure VI.34.

6.3.4 Compressive damage evolutionary analysis of concrete

As it has been explained in several occasions before, to describe the behavior of concrete-filled tube sections is necessary to do also a complementary damage analysis in order to determine the stiffness degradation process of concrete. Damage dissipation energy depends directly on the defined damage evolutionary ratio. It is important to be capable of describing the dissipated energy through compressive damage, with the aim of considering these sections for seismic purposes. To define the damage evolutionary laws for each case, the expressions proposed by Susantha and Ge have been used (Susantha, et al., 2000). This is the reason why damage ratio grows differently according to the B/t proportion. To determine this geometrical percentage, parameter B has been defined as the width of the cell, B_{cell} , and t as the outer plate thickness.

The following sequences show the evolution of the compressive damage ratio in concrete of sections R2, R4 and R9. Note that the differences in the evolution of damage between sections of different B/t ratios are explicit, especially in specimens R4 and R9 [see figures VI.42 and VI.43]. The influence of the thickness on the damage evolutionary ratio is not significant in section R2, owing to the general lack of rigidity of the plates involved [see figure VI.41].

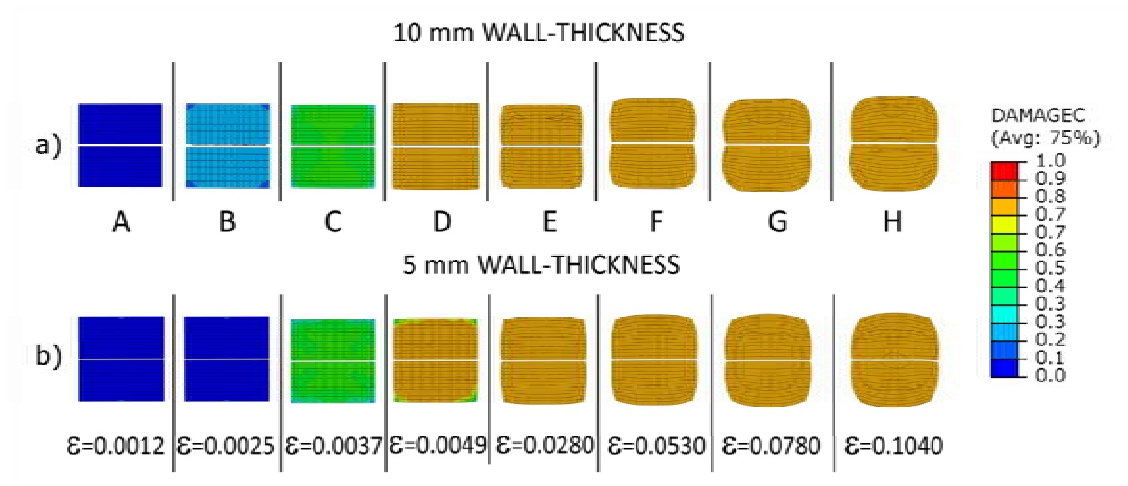


Fig. VI.41 Evolutionary sequence of compressive damage in section R2.
Sections with $B_{cell}/t=40$ [a], and sections with $B_{cell}/t=80$ [b].

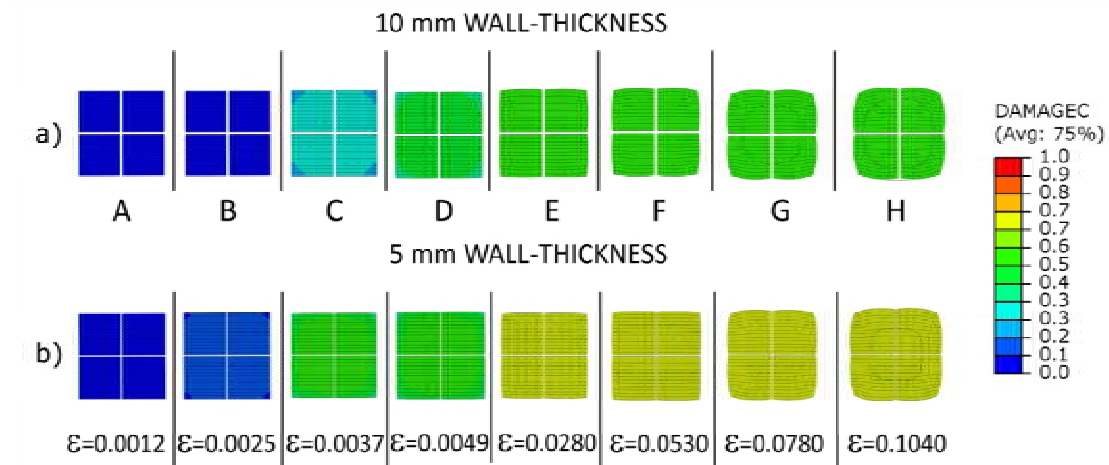


Fig. VI.42 Evolutionary sequence of compressive damage in section R4.
Sections with $B_{cell}/t=20$ [a], and sections with $B_{cell}/t=40$ [b].

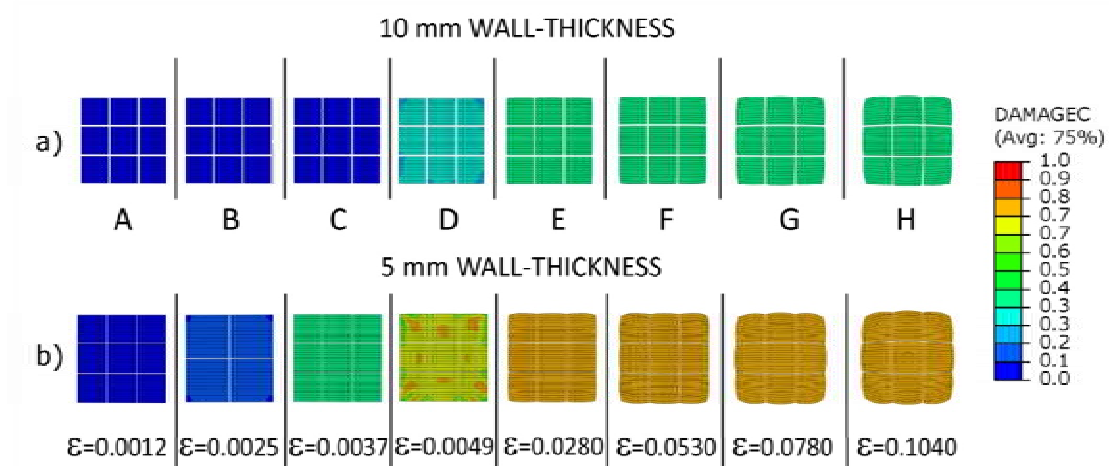


Fig. VI.43 Evolutionary sequence of compressive damage in section R9.
Sections with $B_{cell}/t=20$ [a], and sections with $B_{cell}/t=40$ [b].

Damage in concrete goes closely related with the dissipated energy coming from crushing of mortar. Figure VI.44 shows the evolution of the damage dissipation energy compared to the

evolution of vertical stress in the core; note how energy dissipated by section R2 is more significant than the energy dissipated by section R4. In equivalence of areas, section R2 is really more deformable than section R4; this condition leads directly to more elevated energy dissipation. On the contrary, section R9 shows a value of dissipation energy two times higher than that dissipated by section R4. This is a consequence of the difference of area of concrete between the two typologies. It is obvious that as larger is the area of the core, higher is the damage dissipation energy too.

It is also interesting to see how the damage dissipation energy quickly grows up to point **a** in figure VI.44, coinciding with the descent of softening of concrete. Thus, most part of the damage occurs as a consequence of the softening period, as it can be derived from the curves shown below. While damage energy dissipation occurs sharply in those less stiffened sections, such as R2, this process is slower in those sections which are stiffer, such as R9.

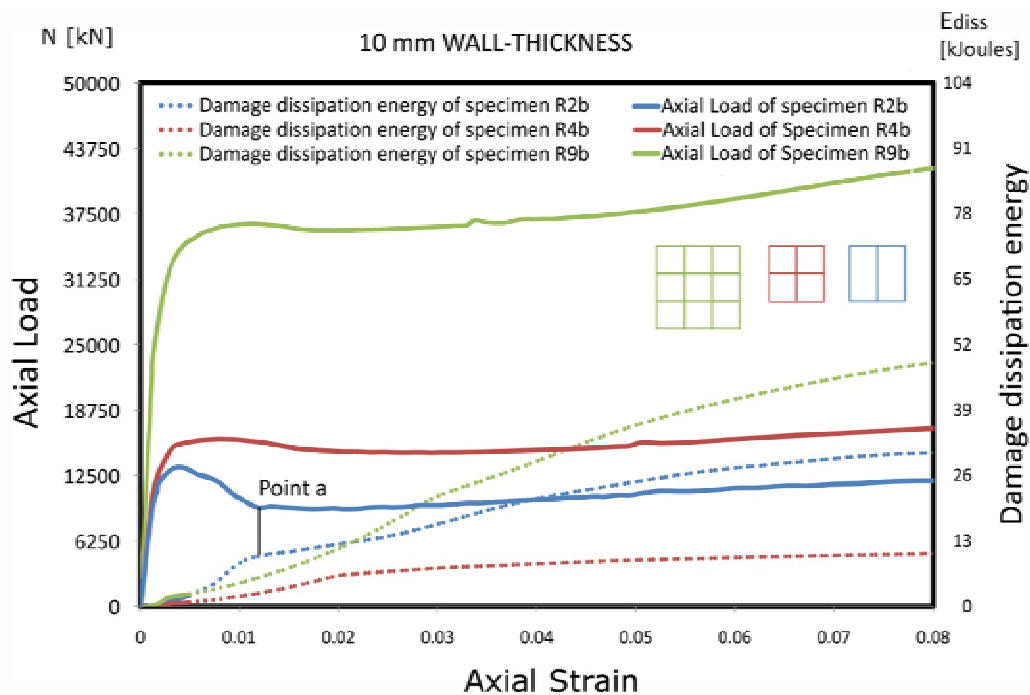


Fig. VI.44 Comparison between damage dissipation energy and vertical stress of concrete.
These diagrams belong to reticulated sections of 10 mm wall-thickness.

Similar as in case of circular sections, the softening period of concrete is intimately related to the evolutionary damage process. As it has been mentioned before, much part of the energy is dissipated during this period [see point **a**, of figure VI.44]; thus, the presence of hydrostatic pressure during this period is important to diminish the load decrement and also the importance of the crushing process. Figure VI.45 clearly shows the evolution of the stiffness degradation of concrete. Major difference between sections R4b and R4e is that the first one does not suffer from softening owing to the rigidity provided by the stiffening plates. The evolutionary process of damage is also delayed in the first case, by showing a different magnitude for stiffness at point C. Point A in figure VI.45 refers to the beginning of damage of concrete and Point B refers to the peak of load. Note that at point B, concrete is already damaged in a 20%.

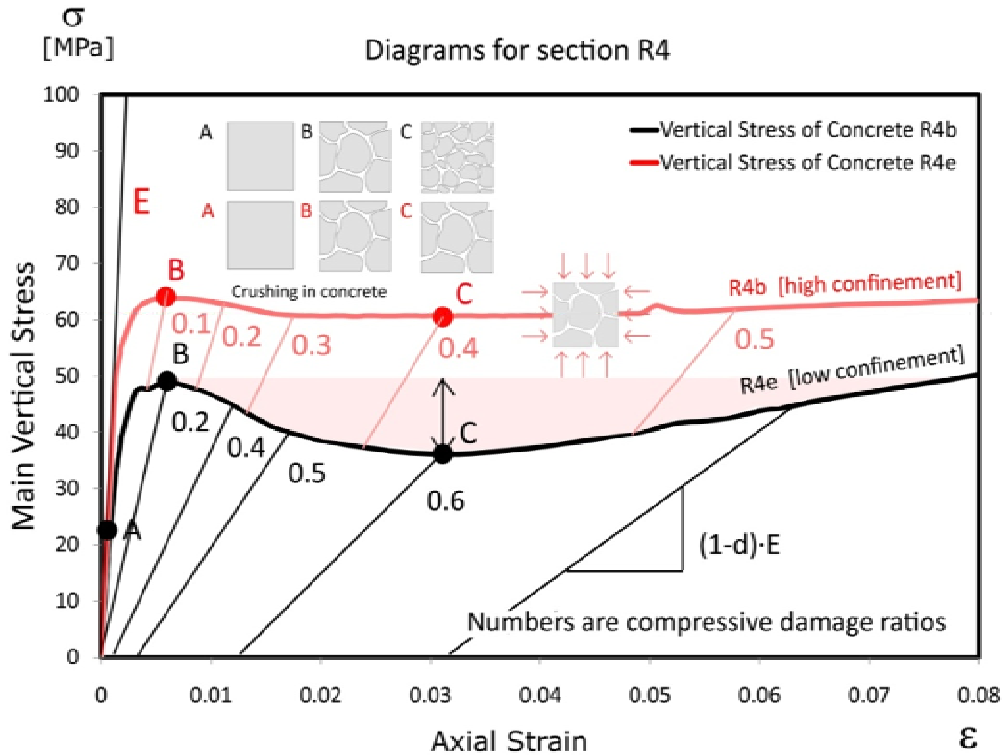


Fig. VI.45 Comparison between vertical stress of concrete and evolution of compressive damage ratio.

Red curve belongs to section R4b [10 mm wall-thickness] and the black curve to section R4e [5 mm wall-thickness].

Figure VI.45 shows the importance of the B/t ratio of the outer tube, not only to enhance the compressive strength of the filling, but also to reduce the importance of the softening period in concrete as a consequence of the confinement effect. The pink-colored area of the diagram shows the loss of load-bearing capacity owing to the deformability of the plates. The numbers shown under the two curves correspond to the damaged stiffness of the core at each stage of loading.

6.3.5 Analysis of contact pressure.

Contact pressure in stiffened square-shaped sections behaves really different from the case of circular CFT sections. The deformability of the plates leads to concentrate normal and friction forces on the edges and intersection points of the tube; as a consequence, most part of concrete is not compressed by the plates [see the blue-colored areas of figure VI.46], except the case of the embedded stiffening plate.

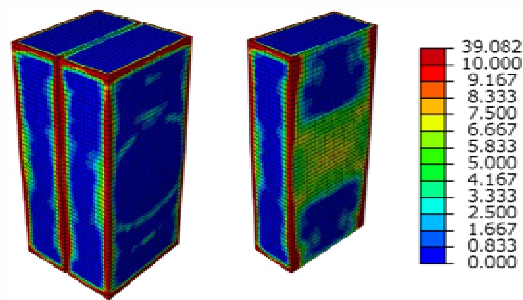


Fig. VI.46 Contact pressure on concrete core, specimen R2, [N/mm²].
The contact pressure is a clear reflex of the confinement provided by the tube.

Different from circular sections, where the pressure provided by the tube is uniformly distributed on the core, in square-shaped sections, contact areas are fully concentrated in specific points of the geometry. This phenomenon is a consequence of the deformability of the plates in the cross-sectional plane, and it leads to a distribution of the pressure in the cross-section in arch effect; as the stiffened edges of the tube are much more rigid than the rest, most part of the load is transferred by these points when concrete expands laterally. The rigidity of these points implies a tensional distribution in the [x] and [y] axes of the cross-sectional plane in arch effect, a fact which leads to a pattern of confinement on the core, according to figure VI.36.

The pressure transferred by stiffening plates on concrete constitutes a clear reflex of the restriction to buckling provided by the core. Central areas of these plates are subjected to high levels of pressure owing to the volumetric expansion of concrete, while the rest is even not compressed [see figure VI.46]

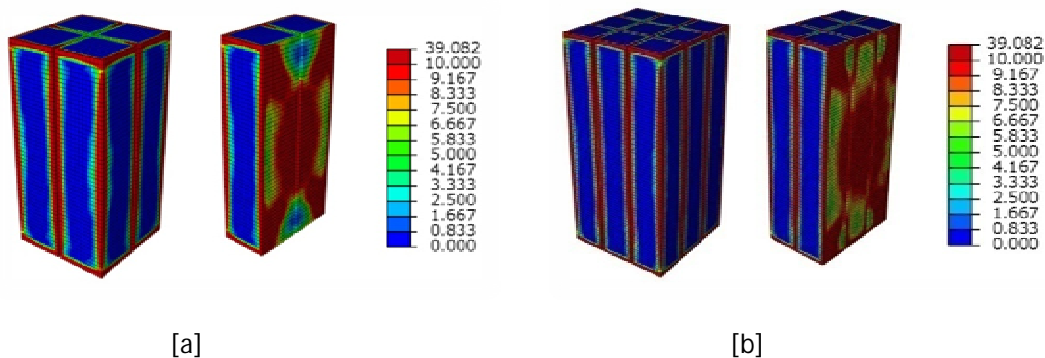


Fig. VI.47 Contact pressure on concrete core in specimens R4 [a] and R9 [b], [N/mm²].
The contact pressure is a clear reflex of the confinement provided by the tube.

Other cases shown in figure VI.47 correspond to sections R4 and R9, in which contact pressure is more uniformly distributed, owing to the rigidity provided by stiffening plates. Note that most part of these plates is compressed in the two cross-sectional axes of the plane, so that tangential stresses can be perfectly transferred. This phenomenon is one of the most interesting strengths of reticulated concrete-filled tubes, since connectors can be avoided in all cases.

